von Karman Institute for Fluid Dynamics

Lecture Series 2025-01

MEASUREMENT, MODELLING AND SIMULATIONS TECHNIQUES FOR NOVEL AIRCRAFT ARCHITECTURES

November 4-6, 2024

SEMI-ANALYTICAL AND LOW-ORDER MODELS APPLIED TO ISOLATED AND INSTALLED PROPULSORS

M. Roger[1] & C. Schram[2]
[1]Ecole Centrale de Lyon, France
[2]von Karman Institute for Fluid Dynamics, Belgium

1 Introduction

The aeroacoustic design of low-noise aerial vehicles is a challenging task, in view of the intricate involved mechanisms of aerodynamic sound generation and propagation. It is only achievable if prediction tools are available, at all steps of the development. Up to that point, numerical approaches based on either the solving of Navier-Stokes equations or the alternative use of LBM (Lattice Boltzmann Methods), possibly used in conjunction with the acoustic analogy, are the only ones able to reach high-fidelity objectives. But they only operate on a predefined geometry, because the physical surfaces must be explicitly meshed prior to the numerical solving. This means that the airframe must already be known to determine the aerodynamic properties and all flow features responsible for the sound. This is not the case at the early design stage, when some details are still unspecified, precisely to allow the exploration of some parameter space for the sake of optimization.

At the lowest level of sophistication, empirical models, usually providing a global information, have been of common use for a long time in engineering. Typically, they establish scaling laws from experimental databases, within classes of machines. The noise from a new machine is estimated by interpolation or extrapolation, with the risk of failing if going out of the acquired database. AI appears as a much more advanced way of addressing the problem, by exploring through very large databases, but with no way to provide physical insight by definition. Analytical approaches are an alternative, expected of intermediate fidelity in the sense that they rely on physics-based mathematical formulations. For tractability, they have to accept drastic geometrical and aerodynamic simplifications, arguing that tiny details most often play a secondary role with regards to the final need of sound predictions in terms of decibels. The question is to what extent they are able to provide a reliable solution, compared to a numerical approach, in the logic of some trade-off between computational cost and time, on the one hand, and accuracy, on the other hand. Typically, human hearing is unable to discriminate sound-level differences of about 1 dB, which corresponds to 10% of error on the amplitude of the sound pressure. As a result, once the aerodynamic forces are recognized as the dominant sources, their amplitude only needs to be determined with the same 10% accuracy. Moreover, useful models for engineering are those which provide the right trends or variations, as the input data are varied, because this is the required quality to efficiently track minimum-noise configurations. As long as the dominant physics is preserved in the simplification process, analytical models can provide relevant estimates. Another aspect is that an analytical model must be developed for each addressed mechanism, which is possible only if this mechanism has been previously identified.

It is also worth noting that in engineering context, the choice of best-suited modeling approach can be declined differently for tonal noise and broadband noise. The sources of tonal noise are deterministic in essence. In the time domain, they are accessible to CFD (Computational Fluid Dynamics) tools, such as Unsteady-RANS simulations. In contrast, random lift fluctuations induced by turbulence, at the origin of broadband noise, can only be reproduced by true unsteady numerical tools, much more expensive. Analytical formulations are usually developed in the frequency-domain, and applied to segments of blades, again for the sake of mathematical tractability. The approach is referred to as strip-theory, an extension of the segmentation performed in the Blade Element Theory (BET). It proceeds by linear superposition principle. The interest is that the same background is

used for tonal noise and for broadband noise.

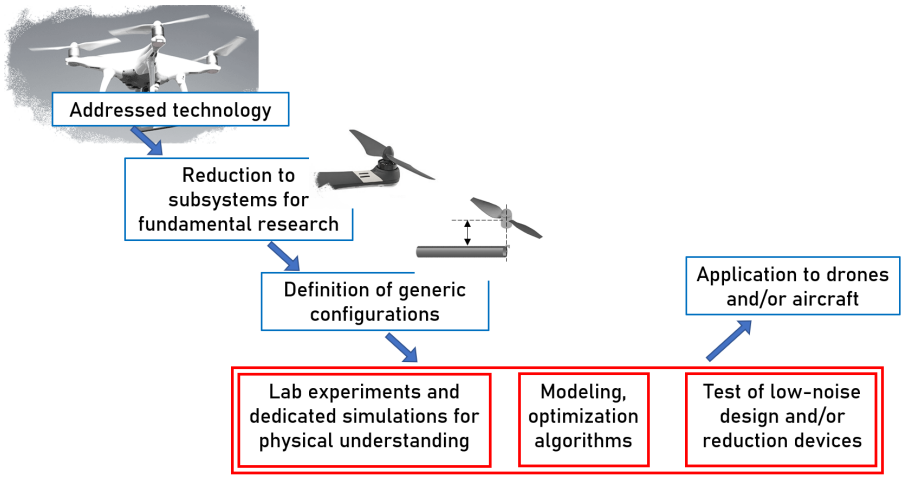


Figure 1: Schematic reduction of a complex technology to generic problems, for focused investigation of fundamental mechanisms.

Figure 1 schematically illustrates what can be considered as a classical way of analyzing aerodynamic sound sources on a complex system, in particular with an analytical view, and with a final objective of noise mitigation. Of course, the same could be made for dedicated experimental investigations, or for focused numerical simulations. The complex system, here a quadrotor drone, is first split into irreducible sub-systems, here propulsive units made of a rotor and a beam. Because the geometry of the beam can still be complex, and because the dominant physics is rather related to gross features, such as beam cross-section and rotor-beam distance, than to other details, a generic configuration is defined. Here, the latter is made of the rotor and a downstream radially positioned cylinder. The interest is that the cylinder is a mathematically tractable geometry, for which fast calculations can be performed. This allows to test numerous values of, say, the diameter of the cylinder and the rotor-cylinder distance, in a relatively short time. Once a minimum noise configuration is found, it can serve as guideline for the redesign of the real, initial sub-system. Of course, the same strategy is applicable to other systems. Typically, the generic configuration illustrated in Fig. 1 also mimics the transmission shaft of the tail rotor of a helicopter.

The present lecture is dealing with mathematical formulations, able to model separately the sources of aerodynamic noise and the sound propagation from these sources, within the scope of the acoustic analogy. In essence, analytical work is aimed at producing closed-form solutions, not resorting to numerical schemes for implementation. The emphasis is put on the tonal noise, even if broadband noise is also shortly addressed.

Whether the free-field sound-pressure formula for the tonal noise is considered in the far-field or in its form uniformly valid everywhere in space, it can be expressed in condensed form as

$$p_{mB}(\mathbf{x}) \;=\; \frac{\mathrm{i}\,k_{mB}}{4\,\pi} \sum_{s=-\infty}^{\infty} \mathcal{P}_s\,F_s\,,$$

where k_{mB} denotes the acoustic wavenumber at the m^{th} multiple of the blade passing

frequency, and $\mathcal{P}_s$ stands for an equivalent transfer function describing the radiation efficiency of the BLH F_s (see the lecture *Review of aeroacoustic analogies and applications to UAM*). A single compact blade segment is considered here. The sound can be predicted only once the BLH F_s are known as source terms, which is a matter of aerodynamics. Furthermore, in cases where the sound radiation must be predicted in the presence of surrounding scattering surfaces, the expression provides the direct field, and the scattered field must still be calculated. This can be done analytically by implementing a tailored Green's function, when the latter is known, or by solving an implicit diffraction problem with a numerical Helmholtz solver. Section 2 is devoted to the determination of equivalent dipole sources distributed on blades, which is directly related to the so-called aerodynamic installation effect introduced in the lecture entitled *Aeroacoustic installation effects in propulsion systems*. Then section 3 addresses the scattering of the direct sound from rotating blades by surrounding surfaces, such as, for instance, the beam supporting a rotor, referred to as the acoustic installation effect.

2 Aerodynamic Installation Effects and Simplified Source Models

The prediction of aerodynamic installation effects is difficult, because it requires not only a realistic description of the three-dimensional flow distortions, but also the determination of the aerodynamic response of the blades operating through the distortions. Even if the three-dimensional mean flow is steady-state, the interaction is unsteady aerodynamics in nature. In that sense, aeroacoustics of rotating blades is very demanding in terms of computational resources if a numerical approach is followed. When analytical means are used instead, the modeling of the distortions and that of the blade response are complementary aspects treated separately, generally based on linear principles. In other words, distortions are described as small disturbances superimposed on an axisymmetrically uniform base flow, and fluctuations of the aerodynamic forces on any blade segment are assumed small compared to the steady-state forces. Apart from that, the steady-state aerodynamics of the blades, in undisturbed conditions, is also needed. Firstly, it gives access to the sources of steady-loading noise and thickness noise. Secondly, it can provide input data for some of the analytical models of flow distortions. Section 2.1 below presents the background for this steady-state aerodynamics. Following sections deal with unsteady aerodynamic models and installation effects.

2.1 The Blade-Element Momentum Theory

The Blade Element Momentum Theory (BEMT) is a combination of two fundamental approaches used in the aerodynamic analysis of rotating blades, particularly in propeller and rotor design:

- Momentum Theory: provides a macroscopic view of the thrust and torque generated by a propeller through the application of conservation laws (mass, momentum, and angular momentum).

- Blade Element Theory: focuses on the blade, dividing it into small radial segments and applying airfoil aerodynamics to each section.

This theory offers a method to estimate the performance of rotating blades, including thrust, torque, and power, by coupling the aerodynamic forces acting on each blade element with the overall momentum changes in the flow.

2.1.1 Momentum Theory

The momentum theory considers the entire rotor or propeller as a thin, idealized disk, known as the actuator disk, which imparts a change in momentum to the airflow. This creates a pressure jump and results in thrust. Due to mass conservation, the stream tube passing through the blade tip trajectory defining the edge of the actuator disk is contracting due to the acceleration of the flow induced by the actuator disk pressure jump (Figure 2).

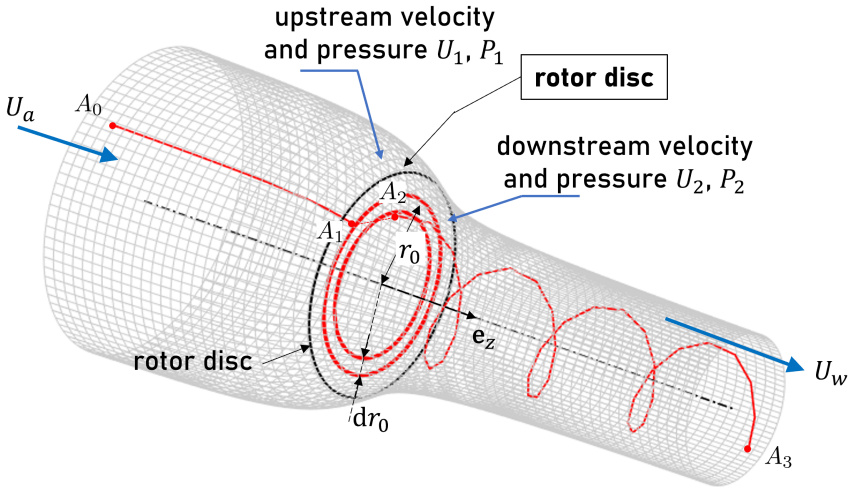


Figure 2: Propeller stream tube, annular strip on the actuator disk and associated steady-state streamlines.

Using the notations of Figure 2, the longitudinal velocities far upstream and downstream of the propeller are U_a and U_w, respectively. The actuator disk is discretized in the radial direction as a succession of annular sections, defining annular stream tubes extending upstream and downstream. For each annulus, the longitudinal induction factor a is defined by $U_1 = (1 + a)\, U_a$. In addition, the propeller induces a swirling motion just downstream of the propeller disk with tangential velocity $a'\,\Omega\, r_0$. The velocity is continuous across each annulus ($U_1 = U_2$) and can be found by equating the thrust that is obtained in two ways:

1. Multiplying the pressure jump across each annulus by its area:

$$\mathrm{d}T = (P2 - P1)\, 2\pi\, r_0\, \mathrm{d}r_0$$

where the pressure difference can be obtained from the Bernoulli equation applies

along the upstream and downstream streamlines:

$$P_\infty + \frac{1}{2}\,\rho\,U_a^2 = P_1 + \frac{1}{2}\,\rho\,U_1^2$$
$$P_\infty + \frac{1}{2}\,\rho\,U_w^2 = P_2 + \frac{1}{2}\,\rho\,U_2^2$$

which can be subtracted to yield

$$P_2 - P_1 = \frac{1}{2}\,\rho\,(U_w^2 - U_a^2)$$

and thus

$$\mathrm{d}T = \frac{\pi}{2}\,\rho\,(U_w^2 - U_a^2)\,r_0\,\mathrm{d}r_0\,. \tag{1}$$

2. From the mass flow rate passing through the actuator disk and net acceleration of the flow:

$$\begin{aligned}\mathrm{d}T &= \dot{m}\,(U_w - U_a)\\ &= 2\pi\,\rho\,r_0\,\mathrm{d}r_0\,(1+a)\,U_a\,(U_w - U_a)\,.\end{aligned} \tag{2}$$

Combining (1) and (2) yields $U_w = (1+2a)\,U_a$, and thus:

$$\begin{aligned}\mathrm{d}T &= 4\pi\,\rho\,r_0\,\mathrm{d}r_0\,a\,(1+a)\,U_a^2\\ &= 4\pi\,\rho\,r_0\,\mathrm{d}r_0\,(U_a + v_{ai})\,v_{ai}\,.\end{aligned} \tag{3}$$

In addition, the conservation of angular momentum gives the relation between the torque induced by each annulus and the resulting tangential velocity:

$$\begin{aligned}\mathrm{d}Q &= 4\pi\,\rho\,r_0^3\,\mathrm{d}r_0\,(1+a)\,U_a\,a'\,\Omega\\ &= 4\pi\,\rho\,r_0^3\,\mathrm{d}r_0\,(U_a + v_{ai})\,U_a\,v_{ti}\end{aligned} \tag{4}$$

The two previous equations provide the thrust and torque of the propeller as functions of the axial and tangential induction factors a and a', or the induced axial and tangential velocities $v_{ai} = a\,U_a$ and $v_{ti} = a'\,\Omega\,r_0$. In order to determine those coefficients, the momentum theory is combined with a model that considers the flow around the blades.

2.1.2 Blade Element Theory

The blade element theory divides the blade into small elements along its radial span. For each element, the local aerodynamic forces (lift and drag) are calculated, based on the local velocity triangle illustrated in Figure 3. In this figure, α is the angle of attack of each blade element, and γ is the pitch (stagger) angle of the blade with respect to the propeller plane.

The lift and drag of each blade element are related to the local angle of attack and relative velocity, the latter being the resultant of the axial component (flight speed plus induced axial velocity) and tangential component (due to the rotation, minus the induced tangential velocity):

$$\begin{pmatrix}\mathrm{d}L\\ \mathrm{d}D\end{pmatrix} = \frac{1}{2}\,\rho\begin{pmatrix}C_L(\alpha)\\ C_D(\alpha)\end{pmatrix} c\,\mathrm{d}r_0\left[(1+a)^2\,U_a^2 + (1-a')^2\,(\Omega\,r_0)^2\right] \tag{5}$$

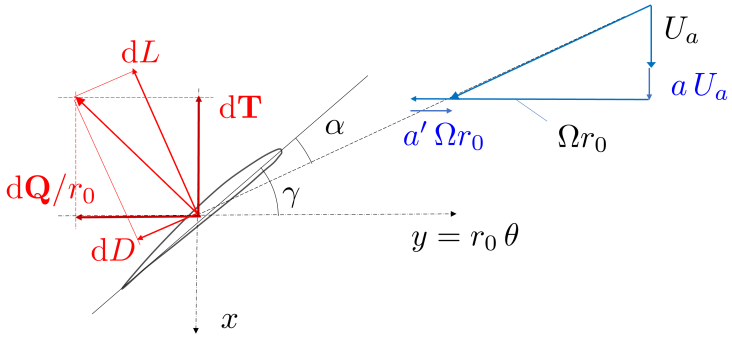


Figure 3: Blade element velocity triangle.

with c the local chord of the blade element. The propeller thrust and torque are then obtained from

$$\begin{pmatrix} \mathrm{d}T \\ \mathrm{d}Q/r_0 \end{pmatrix} = \mathrm{d}L \begin{pmatrix} \cos(\gamma-\alpha) \\ \sin(\gamma-\alpha) \end{pmatrix} + \mathrm{d}D \begin{pmatrix} -\sin(\gamma-\alpha) \\ \cos(\gamma-\alpha) \end{pmatrix} . \tag{6}$$

2.1.3 BEMT Iterative Solution

The set of equations (3), (4), (5) and (6) being non-linearly coupled, an iterative scheme must be followed for its resolution:

1. The induced velocities $v_{ai} = a\,U_a$ and $v_{ti} = a'\,\Omega\,r_0$ are initialized to zero for all annuli.

2. The angle of attack of each blade element is obtained from

$$\alpha = \gamma - \arctan\left(\frac{U_a + v_{ai}}{\Omega\,r_0 - v_{ti}}\right)$$

3. The $C_L(\alpha)$ and $C_D(\alpha)$ are obtained from experimental data, or 2D panel simulations (e.g. using the code XFOIL), etc., and used in (5) to obtain the lift and drag, then the thrust and torque using (6).

4. The momentum equations (3) and (4) are solved (using a non-linear solver) to update the induced velocities v_{ai} and v_{ti}.

5. The algorithm loops back to step 2, until reaching convergence.

Once convergence is reached, the total thrust and torque (hence mechanical power) can be obtained by a radial summation of the annuli. The distributed thrust and tangential forces can as well be used directly to predict the steady-loading noise.

It should however be noted that the above procedure only yields an approximation, which must be corrected for example in order to account for the blade tip effects (downwash induced by the tip vortices). It must also be adapted to cope with a possible misalignment of the incoming flow with respect to the rotation axis (Cerny and Breitsamter, 2020). More accurate models, such as the lifting line theory (Phillips and Snyder, 2000), the lifting surface theory (Schulten, 1996), or three-dimensional unsteady panel methods,

rely on a heavier numerical resolution, but provide more accurate solutions which can also include propeller-airframe installation effects (Hunsaker and Snyder, 2006). These methods are beyond the scope of this course.

2.2 Sinusoidal Airfoil Responses

Analytical models of airfoil unsteady aerodynamics are usually formulated in the frequency domain, and in Cartesian coordinates. They assume small-amplitude and frozen oncoming velocity disturbances, expanded as gusts by Fourier analysis. This requires that the blades of a rotor are radially split into segments and that the annular strip associated with the radial cuts at the bounds of a segment is unwrapped and duplicated to reproduce the angular periodicity. An important result discussed, in particular, by Goldstein (1976) is that, in the linearization limit of small thickness, camber, averaged angle of attack and velocity disturbances, the geometrical parameters and the angle of attack only determine the steady-state aerodynamics, described by classical lift and drag coefficients. But the lift fluctuations, in the scope of an inviscid response, establish independently, as if the airfoil was a zero-thickness flat plate at zero averaged angle of attack, embedded in a flow carrying normal-to-chord velocity disturbances. The latter are equivalent to variations of angle of attack. This decoupling between steady-state aerodynamics and time variations in the linearized theory is a key aspect. It means that lift fluctuations can be determined ignoring the airfoil cross-section design and its classical lift curve. In aeroacoustics, it also suggests that the radiated noise, dominantly attributable to fluctuating lift, can be predicted without precise knowledge of the airfoil shape, except for the special case of rotor steady-loading and thickness noise. This somewhat surprising result explains why quite simple analytical theories can provide reliable acoustic predictions. In analytical approaches, steady-loading noise is addressed separately, as discussed in section 2.1.

Finally, the framework of the linearized theory is to determine the lift fluctuations induced on a flat plate embedded at zero angle of attack in a flow of speed U_0, and submitted to a normal upwash responsible for angle-of-attack variations. This leads to the general sketch in Fig. 4, illustrating what is referred to as Sears' problem in this document. Keeping this in mind, a blade segment must be first assimilated to a flat plate, and equivalent values of U_0 and of the upwash defined at best from the real conditions, usually represented by the velocity triangle introduced later on. This first step can be a matter of ambiguity.

Practically, the lift fluctuations induced on the flat-plate airfoil are determined for each gust of streamwise/chordwise and spanwise aerodynamic wavenumbers, $k_1 = \omega/U_0$ and k_2 respectively. An infinite span is accepted in the problem statement, in order to comply with uniform boundary conditions along the span, for mathematical tractability. This means that the truncation further needed in the applications will ignore end effects. Solving Sears' problem can be attempted in two or three dimensions, based on an either compressible or incompressible framework. Classical solutions, of standard use in aeroacoustics, are shortly described in the next sections.

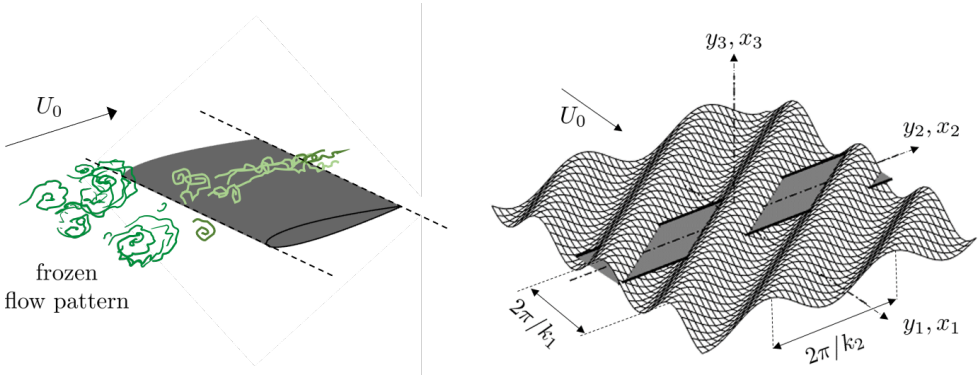


Figure 4: Notations and reference frame for solving Sears' problem in a three-dimensional context. y_i and x_i coordinates will be used to denote source ($y_3 = 0$) and observation points in the following.

2.2.1 Low-Frequency Sears' Theory

Apart from the poorly consistent quasi-steady approximation, except at very low frequencies, the first and simplest solution is the incompressible, two-dimensional one derived by Sears (1941), in the continuation of the work by von Kármán and Sears (1938), based on the theory of potential singularities. The solution provides the complex-valued unsteady lift distribution along the chord of the flat-plate, in the form

$$\ell^S(k_1, y_1, t) \;=\; 2\,\rho_0\,U_0\,\tilde{w}(k_1^*)\,\sqrt{\frac{1-y_1^*}{1+y_1^*}}\,\mathrm{S}^*(k_1^*)\,\mathrm{e}^{-\mathrm{i}\,\omega\,t}\,, \tag{7}$$

where $\tilde{w}$ is the amplitude of the incident gust, $y_1^* = 2\,y_1/c$ is the chordwise coordinate with reference at mid chord, made dimensionless with the half chord, and $k_1^* = k_1\,c/2 = \omega\,c/(2U_0)$ the dimensionless aerodynamic wavenumber of the incident gust in the chordwise/streamwise direction. S^* stands for the complex conjugate of original Sears' function, expressed with Bessel functions of the first and second kinds, as

$$\mathrm{S}^*(k_1^*) \;=\; \frac{2}{\pi\,k_1^*}\,\left([\mathrm{J}_0(k_1^*) - \mathrm{Y}_1(k_1^*)] - \mathrm{i}\,[\mathrm{J}_1(k_1^*) + \mathrm{Y}_0(k_1^*)]\right)^{-1}\,.$$

Integrating Eq. (7) with respect to the chordwise coordinate y_1^* leads to the total unsteady lift force per unit span, for the incident gust of wavenumber k_1^*

$$\tilde{F}(k_1, t) \;=\; \tilde{F}(k_1)\,\mathrm{e}^{-\mathrm{i}\,\omega\,t} \;=\; \pi\,\rho_0\,c\,U_0\,\tilde{w}(k_1^*)\,\mathrm{S}^*(k_1^*)\,\mathrm{e}^{-\mathrm{i}\,\omega\,t}\,.$$

Equation (7) indicates that the lift fluctuations concentrate at the leading edge ($y_1 = -c/2$), with an integrable inverse square-root singularity, and decay to zero at the trailing edge ($y_1 = c/2$). Sears' function is plotted in Fig. 5, superimposed with its approximation

$$\bar{\mathrm{S}}^*(k_1^*) \;=\; \frac{1}{\sqrt{1+2\,\pi\,k_1^*}}\,\mathrm{e}^{\;\mathrm{i}\,k_1^*\left[1\,-\,\dfrac{\pi^2}{2\,(1\,+\,2\,\pi\,k_1^*)}\right]}\,,$$

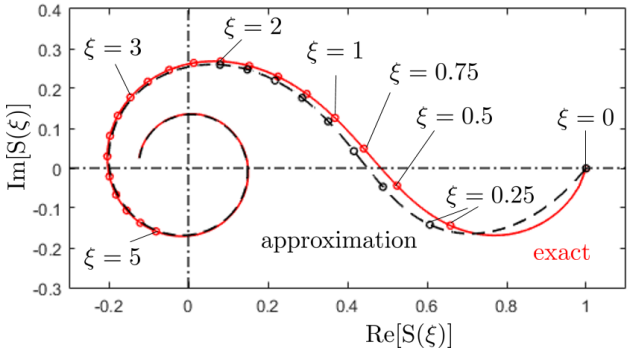


Figure 5: Exact Sears' function (red) and its approximation (dashed black). Values of the argument ξ indicated on the plot.

fairly good as the argument increases. The modulus of Sears' function decays as frequency increases, which means that higher-frequency fluctuations correspond to lower unsteady-aerodynamic efficiency. Furthermore, the phase varies continuously.

Despite its two-dimensional and incompressible limitations, Sears' theory is particularly attractive for analytical investigations of small-size drone rotors. Indeed the latter are often characterized by chord lengths of about 1 cm, and blade-tip Mach numbers of about 0.2. Therefore, the dimensionless frequency parameter $\mu = k_1^* M_0/\beta^2 = kc/(2\beta^2)$, where $\beta^2 = 1 - M_0^2$, $M_0 = U_0/c_0$ being the Mach number, close to the Helmholtz number based on the half-chord, approaches 1 only around 10 kHz. This means that the chord is acoustically compact, in which case Sears' theory is reliable. In practice, Sears' theory is considered acceptable for acoustic predictions, as long as μ is smaller than, say, 0.4-to-0.75[1]. Larger rotors of eVTOL aircraft may require extensions to higher dimensionless frequencies, described in the next section.

2.2.2 High-Frequency Amiet's Theory

For non-compact chords, propagation-path differences between points at leading and trailing edges are no longer negligible, and phase-lags of the induced lift forces are also induced by oncoming gusts, neglected in Sears' theory. Equivalently, compressibility effects become significant in the airfoil response. Amiet's theory is the most commonly used alternative in this case, because its three-dimensional and compressible essence makes it physically very consistent. It is shortly described in this section. Details can be found in original papers by Amiet (1975) and Paterson and Amiet (1976), as well as in more recent extensions and assessment (see for instance Roger (2013) and Roger and Moreau (2010)).

Depending on the obliqueness of the incident gust, the interaction can travel along the leading edge at either sub-sonic or supersonic speed. The gust is said sub-critical or supercritical, respectively. This is defined by the ratio of spanwise k_2 and streamwise k_1

[1]The two-dimensional restriction makes the theory unable to predict the response to oblique gusts. Use can be made of Graham's similarity rules in this case to derive a correction, not detailed here. See Graham (1970)

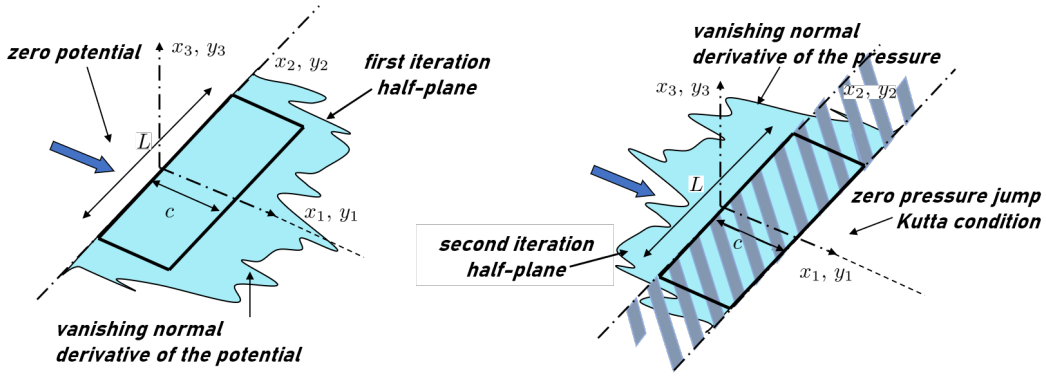


Figure 6: Illustration of the two iterations in Amiet's theory. The induced lift is obtained on the hatched infinite strip. Only the values on the rectangle of finite-span L mimicking the airfoil are retained as sound sources.

wavenumbers and is expressed by the gust parameter

$$\Theta \;=\; \frac{k_1^* M_0}{k_2^* \beta}\,.$$

In the present three-dimensional context, the full solution for the distributed unsteady lift of supercritical oblique gusts including main leading-edge impingement and trailing-edge back-scattering reads (Mish and Devenport (2006), Roger (2010))

$$\tilde{\ell}(y_1,y_2) \;=\; \ell(y_1,y_2,t)\,\mathrm{e}^{\mathrm{i}\,\omega\,t} \;=\; \frac{2\,\rho_0\,U_0\,\tilde{w}\,\mathrm{e}^{\mathrm{i}\,\pi/4}}{\sqrt{2\,\pi\,(k_1^*+\beta^2\kappa)}}\,\mathrm{e}^{\mathrm{i}\,k_2^*\,y_2^*}$$

$$\times\left\{1-\sqrt{\frac{2}{1+y_1^*}}-(1-\mathrm{i})\,\mathrm{E}\,\left[2\,\kappa\,(1-y_1^*)\right]\right\}\,\mathrm{e}^{-\mathrm{i}\,(M_0\,\mu-\kappa)\,(1+y_1^*)}\,,$$

introducing the non-dimensional chordwise coordinate y_1^* with origin at the center chord, and the notation $\kappa \;=\; \mu\,\sqrt{1-1/\Theta^2} \;=\; \sqrt{\mu^2-{k_2^*}^2/\beta^2}$. E is a Fresnel integral defined as

$$\mathrm{E}(\xi) \;=\; \int_0^{\xi}\frac{\mathrm{e}^{\,\mathrm{i}\,t}}{\sqrt{2\,\pi\,t}}\,\mathrm{d}t\,.$$

For sub-critical gusts, κ is replaced by $\mathrm{i}\,\kappa'$ with $\kappa' = \sqrt{({k_2^*}^2/\beta^2)-\mu^2}$ and the term $(1-\mathrm{i})\,\mathrm{E}$ by the error function erf $([2\,\kappa'\,(1-y_1^*)]^{1/2})$. All gusts involve the integrable inverse square-root singularity at the leading edge already pointed out in Sears's solution.

The far-field radiation for a single gust is expressed in a reference frame attached to the airfoil as

$$\tilde{p}(\mathbf{x},\omega) \;=\; -\,\frac{i\,k\,c\,\rho_0\,x_3}{2\,S_0^2}\,U_0\,\tilde{w}\,L\,\frac{\sin[\,L\,(k_2^*-k^*\,x_2/S_0)/c]}{L\,(k_2^*-k^*\,x_2/S_0)/c}\,\mathcal{L}\,, \tag{8}$$

with $k^* \;=\; kc/2$, where the sine-cardinal function $\sin\xi/\xi$ represents the span-wise radiation integral and where the non-dimensional chord-wise radiation integral (or aeroacoustic

transfer function) $\mathcal{L}$ is introduced as

$$\mathcal{L}\,(\mathbf{x}, k_1, k_2) \;=\; \int_{-1}^{1} \frac{\ell(y_1^*, y_2^*)\,\mathrm{e}^{-\mathrm{i}\,k_2^*\,y_2^*}}{2\,\pi\,\rho_0\,\tilde{w}}\,\mathrm{e}^{\mathrm{i}\,\mu\,(M_0 - x_1/S_0)\,y_1^*}\,dy_1^*\,.$$

In the expressions, (x_1, x_2, x_3) stand for observer's coordinates with origin at the center of the airfoil, respectively in the stream-wise, span-wise and normal directions. $S_0 = [x_1^2 + \beta^2\,(x_2^2 + x_3^2)]^{1/2}$ is a corrected distance accounting for sound convection by the surrounding flow. It is close to the geometrical distance R only if M_0 is small. L is the span. The sine-cardinal function accounts for the span-wise interference associated with the wavenumber k_2.

The function $\mathcal{L}$ has different expressions for the sub-critical and supercritical gusts, including leading-edge and trailing-edge contributions: $\mathcal{L} = \mathcal{L}_1 + \mathcal{L}_2$. For supercritical gusts it reads (Roger (2010))

$$\mathcal{L}_1 \;=\; -\,\frac{1}{\pi}\,\sqrt{\frac{2}{(k_1^* + \beta^2\,\kappa)\,\Theta_4}}\,\mathrm{e}^{-\mathrm{i}\,\Theta_2}\,\mathrm{E}\,[2\,\Theta_4]\;, \tag{9}$$

$$\mathcal{L}_2 \;=\; \frac{\mathrm{e}^{-\mathrm{i}\,\Theta_2}}{\pi\,\sqrt{2\,\pi\,(k_1^* + \beta^2\,\kappa)}\,\Theta_4} \tag{10}$$

$$\times\,\left\{\mathrm{i}\,(1 - \mathrm{e}^{2\,\mathrm{i}\,\Theta_4}) \;-\; (1 + \mathrm{i})\,\left[\mathrm{E}(4\,\kappa) \;-\; \mathrm{e}^{2\,\mathrm{i}\,\Theta_4}\,\sqrt{\frac{2\,\kappa}{\Theta_3}}\,\mathrm{E}\,[2\,\Theta_3]\right]\right\}\;,$$

with $\Theta_2 = \mu\,(M_0 - x_1/S_0) - \pi/4$, $\Theta_3 = \kappa + \mu\,x_1/S_0$, $\Theta_4 = \kappa - \mu\,x_1/S_0$.

For sub-critical gusts the expressions follow as

$$\mathcal{L}_1 \;=\; -\,\frac{1}{\pi}\,\sqrt{\frac{2}{(k_1^* + \mathrm{i}\,\beta^2\,\bar{\kappa}')\,\Theta_4'}}\,\mathrm{e}^{-\mathrm{i}\,\Theta_2}\,\mathrm{E}\,[2\,\Theta_4']\;, \tag{11}$$

$$\mathcal{L}_2 \;=\; \frac{-\,\mathrm{e}^{-\mathrm{i}\,\Theta_2}}{\mathrm{i}\,\pi\,\sqrt{2\,\pi\,(k_1^* + \mathrm{i}\,\beta^2\,\bar{\kappa}')}\,\Theta_4'} \tag{12}$$

$$\times\,\left\{1 - \mathrm{e}^{2\,\mathrm{i}\,\Theta_4'} \;-\; \mathrm{erf}(\sqrt{4\,\kappa'}) \;+\; 2\,\mathrm{e}^{2\,\mathrm{i}\,\Theta_4'}\,\sqrt{\frac{\kappa'}{\Theta_3'}}\,E\,[2\,\Theta_3']\right\}\;,$$

with $\Theta_4' = \mathrm{i}\,\kappa' - \mu\,x_1/S_0$, $\Theta_3' = \mathrm{i}\,\kappa' + \mu\,x_1/S_0$. These expressions are given for completeness and because they help to define the ability of some flow patterns to radiate sound. But their interest is limited for applications to rotors, because they express the field in a reference frame attached to an airfoil, thus a single blade segment. Either a transposition is needed (case of some broadband-noise models), or the local unsteady lift is directly used for implementation of the general formulae of tonal noise, as explained below.

The interest of solving the high-frequency problem with iterative half-plane wave-scattering intermediate solutions is that technological effects can be introduced easily. Leading-edge sweep is one of them, and spanwise variations of chord are another one, by assuming different sweep angles at both edges, each being treated in different sets of Cartesian coordinates. In rotating-blade noise applications, this leads to assimilate blade

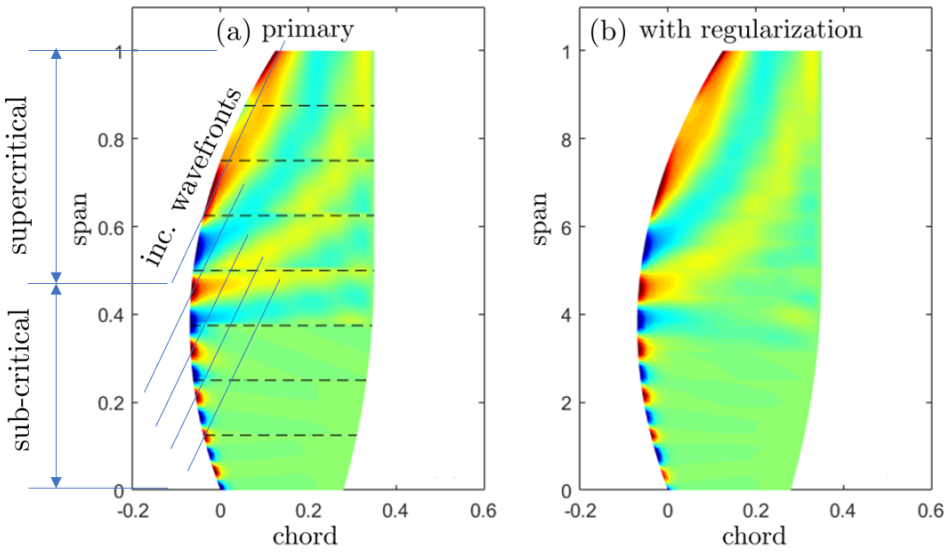


Figure 7: Instantaneous lift induced on a non-compact blade by an incident oblique gust. (a) adjacent blade-segment responses; incident gust wavefront indicated by the oblique lines. (b): continuous lift distribution after regularization.

segments to trapezoids, as proposed by Carazo et al. (2011). In fact, Amiet's theory provides two outputs. The first one is the induced lift on any segment assimilated to a flat plate, per gust, as a generalization of Sears' theory. The second one is the far-field sound radiated by the considered gust and segment, in the reference frame of the segment, of no direct use for rotor noise calculations. Only the distributed unsteady lift defines the BLH to be considered as input in the far-field rotor-noise formula. Applications to the tonal noise from non-compact blades is delicate, because adjacent segments are treated separately in the strip-theory approach, whereas the whole blade surface is a coherent source distribution. Special procedures can need to be developed to generate a continuous lift distribution, in phase and amplitude, to be projected back onto the mean-camber surface of the blades and discretized for sound calculations. Such a procedure, described by Carazo et al. (2011), is illustrated in Fig. 7, and details are found in the reference. Figure 7-a shows the raw lift responses of 8 segments, for an incident oblique gust. The hydrodynamic wavefronts of the gust are indicated by the oblique lines. They are nearly parallel to the leading edge in the blade tip region, so that the local gust impingement remains supercritical on the top 4 or 5 segments. Closer to the hub, on the lower 3 to 4 segments, the local skewness angle is larger and the local gust impingement is subcritical. The unsteady lift concentrates at the very leading edge and rapidly drops farther downstream along the chord. For this gust, logically, the lower part of the blade poorly contributes to the radiated noise, whereas the contribution from the upper 2/3 dominates. The regularization is only required for extremely non-compact blades, for which the size of the mesh elements must be defined smaller than the span of each segment and multiple elements are needed along both the span and the chord of the segments. It prevents errors due to the discontinuities between adjacent segments.

In cases where the chord is compact, the blade is only discretized in the spanwise direction, as a line array of equivalent point dipoles, and no smoothing procedure is needed. This is the usual framework of drone blades at subsonic Mach numbers, for the first harmonics of the BPF. Sears' theory is used instead of Amiet's.

2.2.3 High-Frequency Broadband-Noise Modeling

The expression, Eq. (8), is the elementary deterministic solution for rotor tonal-noise predictions due to periodic variations of the angle of attack on the blades. It also allows to model the broadband noise due to random variations, such as produced by upstream turbulence, at the price of an additional statistical formulation. This part of the acoustic signature is called turbulence-impingement noise (TIN). Typically, for drone rotors, tonal noise dominates the spectrum at low-to-mid frequencies, so that broadband noise is of major interest at high frequencies, much higher than the rotational frequency in practice. The turbulence at the origin of broadband noise is characterized by short coherence times. The contribution of a blade segment to the sound at some point, from a given angular position along the segment path, is not correlated to contributions from other angles[2]. It can be assimilated to what the segment would emit if in rectilinear motion locally tangent to the circular motion, as shown by Sinayoko et al. (2013). The configuration is sketched in Fig. 8. The rectilinear-motion contribution is expressed in the reference frame of the segment, then corrected to account for the Doppler effect of the relative motion towards the observer. The total far-field pressure PSD in the rotor axes $(\mathbf{e}_X, \mathbf{e}_Y, \mathbf{e}_Z)$ is obtained as

$$S_{pp}^{T}(\mathbf{x}, \omega) \;=\; \frac{B}{2\,\pi} \int_0^{2\,\pi} \left(\frac{\omega_e(\varphi)}{\omega} \right)^2 \, S_{pp}^{\varphi}(\mathbf{x}, \omega_e) \, \mathrm{d}\varphi \,, \tag{13}$$

with the inverse Doppler factor

$$\frac{\omega_e(\varphi)}{\omega} \;=\; 1 + \frac{\Omega\, r}{c_0} \, \sin\varphi \, \sin\Theta \,,$$

if $S_{pp}^{\varphi}(\mathbf{x}, \omega_e)$ refers to the PSD in the reference frame of the segment, of axes $(\mathbf{e}_1, \mathbf{e}_2, \mathbf{e}_3)$, at angle $\varphi = \Omega t$, according to one of the analytical models presented in what follows. For such a model, the observer is assumed at rest and the fluid is assumed to move uniformly at some chordwise velocity U_0, assuming a non-zero angle of attack. This condition is necessary for the mathematical statement of Sears' problem, even if not realistic. The formula implicitly assumes that the propagation medium is at rest in the rotor reference frame. Fast and quite accurate predictions are ensured this way, if reliable input statistics of the incriminated turbulence is available. Usually, the turbulence is assumed nearly homogeneous and isotropic, at least locally in the region where the interaction takes place. Typically, models of von Kármán or Liepmann are tuned on the local turbulent intensity w_{rms}/U_0 and integral length scale Λ, needed as input data.

The isolated-airfoil noise problem is stated in Cartesian coordinates, for a rectangular flat-plate airfoil, assuming homogeneous flow conditions along the span. This is required for mathematical tractability but is not compatible with the radially increasing tangential

[2]An exception is the case of blade-to-blade correlations induced as the blades are chopping very elongated turbulent eddies, a case not considered here.

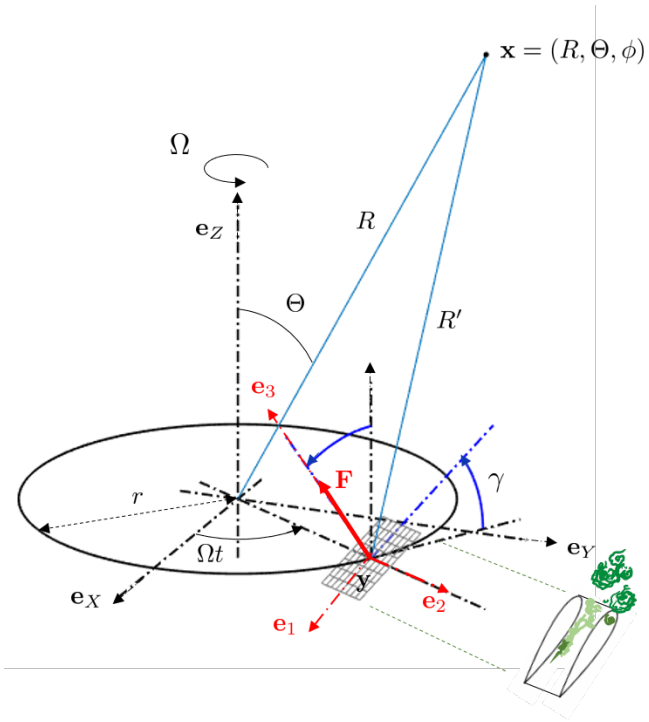


Figure 8: Reference frames used to transfer isolated-airfoil noise models to rotating blade segments.

speed of a blade segment associated with rotating motion. This is why the modeling has to rely on a strip theory, according to which a blade is split into segments in the spanwise direction and approximated by an airfoil in each strip. Now going to the solving procedure for a single segment or airfoil, the fluctuating lift and the resulting far-field pressure are stationary random quantities, the description of which relies on associated power spectral densities. Therefore, the sound is expressed through the PSD $S_{pp}(\mathbf{x}, \omega) = \tilde{p}(\mathbf{x}, \omega)\, \tilde{p}^*(\mathbf{x}, \omega)$, the Fourier transform of the pressure $\tilde{p}$ being obtained by summing contributions from all surface points on the airfoil surface. This implies that the key information on the source is the two-points statistics of lift fluctuations, which can be transposed onto the statistics of the incident velocity gusts. More precisely, the two-wavenumber turbulence spectrum of the upwash velocity component is needed. Details of the derivations are given by Amiet (1975) and by Paterson and Amiet (1976). Only formulae for practical implementation are given in this section.

After derivations, the S_{pp} of TIN is obtained as

$$S_{pp}(\mathbf{x}, \omega) = \left(\frac{k\, \rho_0\, c\, x_3}{2\, S_0^2}\right)^2 \pi\, U_0\, \frac{L}{2} \int_{-\infty}^{\infty} \left[\Phi_{ww}\left(\frac{\omega}{U_0}, k_2\right) \right.$$

$$\left. \times \left| \mathcal{L}\left(x_1, \frac{\omega}{U_0}, k_2\right) \right|^2 \frac{\sin^2\left[\left(\frac{k\, x_2}{S_0} - k_2\right) \frac{L}{2}\right]}{\pi\, \frac{L}{2} \left(\frac{k\, x_2}{S_0} - k_2\right)^2} \right] \mathrm{d}k_2\,. \tag{14}$$

The notation $\Phi_{ww}(k_1, k_2)$ denotes the two-wavenumber spectrum for the special

streamwise aerodynamic wavenumber $k_1 = K_1 = \omega/U_0$, imposed by the assumption of frozen vorticity. The transfer function $\mathcal{L}$ expresses the chordwise/streamwise response to the incident turbulence, detailed gust by gust. It involves observer's coordinate x_1 and is therefore not only a matter of chordwise non-compactness but also a matter of projected position in the mid-span plane. The cardinal sine function expresses spanwise non-compactness, which is a matter of wavenumber k_2 combined with observer's coordinate off the mid-span plane. The practical implementation of the formula requires some explicit expressions for Φ_{ww} and for $\mathcal{L}$. A choice often made in the von Kármán model, according to which

$$\Phi_{ww}(k_1,k_2) \;=\; \frac{4\,w_{rms}^2}{9\,\pi\,k_e^2}\,\frac{\left(\dfrac{k_1}{k_e}\right)^2+\left(\dfrac{k_2}{k_e}\right)^2}{\left[1+\left(\dfrac{k_1}{k_e}\right)^2+\left(\dfrac{k_2}{k_e}\right)^2\right]^{7/3}}\,, \qquad k_e \;=\; \frac{\sqrt{\pi}}{\Lambda}\,\frac{\Gamma(5/6)}{\Gamma(1/3)}\,.$$

For large values of the aspect ratio L/c, thus $L \to \infty$, the sine-cardinal function of Eq. (14) can be approximated by a Dirac delta function, and the simpler following formula is obtained:

$$S_{pp}(\vec{x},\omega) \;=\; \left(\frac{\rho_0\,k\,c\,x_3}{2\,S_0^2}\right)^2\,\pi\,U_0\,\frac{L}{2}\,\Phi_{ww}\left(\frac{\omega}{U_0},\frac{k\,x_2}{S_0}\right)\,\left|\mathcal{L}\left(x_1,\frac{\omega}{U_0},\frac{k\,x_2}{S_0}\right)\right|^2\,. \qquad (15)$$

Tests indicate that this approximation is relevant for aspect ratios larger than, say, 2.5. It appears that, always in the reference frame of the considered segment, the sound at point $\mathbf{x}$ and angular frequency ω is only attributable to the unique gust of wavenumbers

$$k_1 \;=\; K_1 \;=\; \frac{\omega}{U_0}\,, \qquad\qquad k_2 \;=\; K_2 \;=\; \frac{\omega x_2}{c_0 S_0}\,,$$

this gust being always supercritical. In contrast, the exact expression, Eq. (14), involves both sub- and supercritical gusts. This point is discussed, for instance, by Roger (2013). The best practice for spanwise blade splitting is an open question. The span of each segment should be larger than the local correlation length of the incident turbulence, but too large aspect ratios are obviously questionable. A special elegant method was proposed by Christophe et al. (2008) to ensure relevant predictions.

Another interest of Amiet's theory, in its statistical form, is that it can be transposed to the modeling of trailing-edge noise, with the same iterative strategy on half-plane problems (see Amiet (1976) and Roger and Moreau (2005)). The difference is that now, the first iteration represents the scattering of boundary-layer turbulence as sound at the trailing-edge, by virtue of the Kutta condition. The second iteration accounts for leading-edge back-scattering; it is only important for quite small chords, and ensures more realistic predictions, even for blade chords approaching compactness. The conditions for application are that the turbulence is defined by its hydrodynamic wall-pressure field closely upstream of the trailing edge, and that it remains attached, so that a convection speed can be defined in the streamwise direction. The case of small-size drone rotor blades is somehow questionable, for two reasons. Firstly, Amiet's trailing-edge noise model is beyond its validity scope for compact blade chords. Secondly, the boundary-layer turbulence is often triggered by a laminar separation bubble, which is a recognized effect of low

Reynolds numbers. The statistical properties of such a flow regime are *a priori* much less known than those at higher Reynolds numbers.

The PSD of the far-field acoustic pressure for trailing-edge noise reads

$$S_{pp}(\mathbf{x},\omega) \;=\; \left(\frac{k\,x_3\,L\,c}{4\,\pi\,S_0^2}\right)^2 \;\frac{2}{c}\;\int_{-\infty}^{\infty} \Pi_0(\frac{\omega}{U_c},k_2^*)\,\frac{\sin^2\left\{\dfrac{L}{c}\,(k_2^*-k^*\dfrac{x_2}{S_0})\right\}}{\left\{\dfrac{L}{c}\,(k_2^*-k^*\dfrac{x_2}{S_0})\right\}^2}\;\left|I(\frac{\omega\,c}{2\,U_c},k_2^*)\right|^2\;\mathrm{d}k_2^*\,. \tag{16}$$

It is written here in dimensionless variables, introducing the wavenumber spectrum of the wall-pressure fluctuations

$$\Pi_0(\frac{\omega}{U_c},k_2^*) \;=\; \frac{1}{\pi}\,\Phi_{pp}(\omega)\,\ell_y(k_2^*,\omega)\,,$$

where $\Phi_{pp}(\omega)$ is the wall-pressure PSD induced closely upstream of the trailing edge by the incident turbulence only (ignoring contamination by the Kutta condition) and $\ell_y(k_2^*,\omega)$ is the correlation length defined from the coherence function between two span-wise locations η_2 apart from each other as

$$\ell_y(k_2^*,\omega) \;=\; \int_0^{\infty} \sqrt{\gamma^2(\eta_2,\omega)}\,\cos(k_2\,\eta_2)\,\mathrm{d}\eta_2\,.$$

The associated long-span approximation reads

$$S_{pp}(\mathbf{x},\omega) \;=\; \left(\frac{k\,x_3 c}{2\,\pi\,S_0^2}\right)^2\,\pi\,\frac{L}{2}\;\left|I(\frac{\omega\,c}{2\,U_c},k^*\frac{x_2}{S_0})\right|^2\;\Pi_0(\frac{\omega}{U_c},k^*\frac{x_2}{S_0})\,. \tag{17}$$

The key practical issue is to get a relevant information on $\Phi_{pp}(\omega)$ and $\ell_y(k_2^*,\omega)$. Facing the large variety of flow topology and regimes on rotating blades, the best approach for engineering is still to rely on empirical scaling laws, established from thorough experimental databases or less often by computations. This was investigated many times since the first attempts of TEN modeling, and remains a matter of debate, for what are the best parameters to use for scaling data. In the case of re-attached boundary layers after laminar separation on the low-Reynolds drone blades, reliable data are often missing. Anyway, the choice of a model is also depending on what is available in terms of boundary-layer description. The reader can find advances and reviews in the papers by Rozenberg et al. (2012), Lee (2018), Grasso et al. (2019), and by Bertagnolio et al. (2017) for airfoils with separated flows. Machine learning was also recently proposed to model $\Phi_{pp}(\omega)$ by Arroyo Ramo et al. (2024). Again, as discussed by Moreau and Roger (2009), the large-span approximation is reliable for aspect ratios larger than 2.5.

2.3 Flow Distortions

Many kinds of distortions are encountered in rotating blade aeroacoustics, as pointed in the lecture *Aeroacoustic installation effects in propulsion systems*, leading to consider that each addressed case is special, characterized by almost unique distortion features to

cope with. In analytical approaches, generic distortions must be defined, ideally classes of distortions, so that the same model could be used within a given class by just changing the parameters. This is a limitation of the approach. In this section, basic models are outlined, each addressing a well identified kind of distortion, such as the potential flow around an obstacle, the edgewise flow due to advancing flight, the ingestion of a ground vortex and so on. It is understood that numerical means are not affordable or unable to run in the considered situation, and that the model distortion is just an approximation, incomplete in essence; yet it provides physical insight and is able to define guidelines or best engineering practice.

2.3.1 Edgewise Flow on a Rotor

The main effect of advancing flight for a rotor is to combine the tangential blade motion with an edgewise flow component. The relative angle of attack on a blade segment varies cyclically, with maximum and minimum relative speeds for the advancing and retreating phases of the blade motion, respectively. This is illustrated in Fig. 9 for a single blade segment, in a quite ideal view.

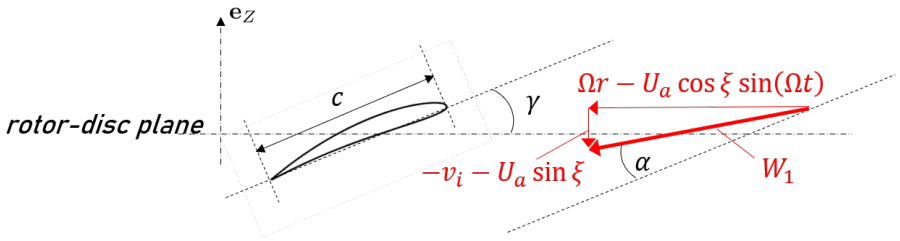


Figure 9: Comprehensive sketch of the combined effects of rotating blade motion and negative-pitch advancing flight, on the velocity triangle.

The expressions of the instantaneous relative velocity and angle of attack can be derived as

$$W_1(t) \;=\; \left[(U_a \,\sin\xi + v_i)^2 + (\Omega r - U_a \,\cos\xi \,\sin(\Omega t))^2\right]^{1/2} ,$$

$$\alpha(t) \;=\; \gamma - \tan^{-1}\left(\frac{U_a \,\sin\xi + v_i}{\Omega r - U_a \,\cos\xi \,\sin(\Omega t)}\right) ,$$

v_i being the induced velocity and ξ the pitch angle of the nose-down attitude. Now the possible ambiguity in the definition of an equivalent Sears' problem, is that the mean velocity is not aligned with the chord (non-zero averaged angle of attack), and that the disturbance vector of the velocity triangle is not perpendicular to the chord. Furthermore, the variations of the relative velocity around the mean value are not small, questioning the validity of a linearized approach. There is not a unique way of defining an 'almost' equivalent Sears' problem. For instance, the chordwise velocity U_0 can be defined as the projection of the averaged W_1 along the chord line. But considering the chordwise trace speed of the disturbances also makes sense. Trying both could be a way of defining a margin of error, inherent to analytical modeling. Anyway, the upwash $w(t)$ is obtained by projection, as

$$w(t) \;=\; W_1(t) \,\sin\alpha(t) \,.$$

A Fourier series is then performed to get the distortion harmonics w_s:

$$w(t) \;=\; \sum_{s=-\infty}^{\infty} w_s \, \mathrm{e}^{-\mathrm{i}\, s\, \Omega t} \,, \qquad w_s \;=\; \frac{\Omega}{2\pi} \int_0^{2\pi/\Omega} w(t) \, \mathrm{e}^{\mathrm{i}\, s\, \Omega t} \, \mathrm{d}t \,.$$

Finally, if the blade chord is acoustically compact, so that Sears' theory is relevant, the blade-loading harmonics are obtained as

$$F_s \;=\; \pi \rho_0 \, c \, U_0 \, \Delta r \, w_s \, \mathrm{S} \left(\frac{s \, \Omega c}{2 \, U_0} \right) \,.$$

Amiet's formalism should be used instead, for non-compact blades.

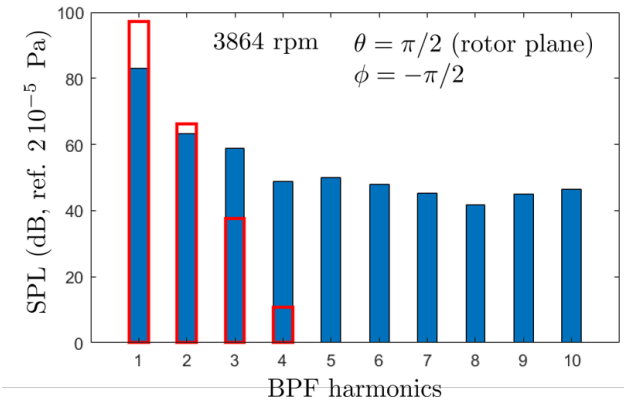


Figure 10: Tonal noise spectrum of the front starboard rotor of the numerical test case of Misiorowski et al. (2019), as deduced from computed thrust coefficients (blue) and as predicted by the analytical model (empty red). Observer in the rotor plane.

As an example, let's consider again the test-case of Misiorowski et al. (2019) addressed in the lecture *Aeroacoustic Installation Effects*, and compare what this simple analytical model provides as prediction to the post-processing of numerical results. For this, the same far-field expression of the tonal noise is used. The results are reported in Fig. 10. Large overall discrepancies are observed. In particular, the BPF is overestimated with the analytical prediction of the BLH. This could be due to the fact that a simplistic BEMT model for hover is used to infer the steady-loading, known to be significant at the BPF, and that the presently estimated induced velocities are deduced from this BEMT. They are suspected to be questionable in the present forward-flight configuration. Moreover, for what is dealing with the higher harmonics, the present model assumes an isolated rotor, whereas the configuration is extracted from the numerical simulation of a complete quadrotor, thus including also rotor-rotor aerodynamic interactions. Blade-tip effects are also ignored here. The best agreement is obtained at 2BPF, a tone for which steady-loading noise is of secondary importance. The Bessel-function weighting makes that the most efficient BLH is of order 4, but its amplitude is probably very small. The strongly dominant BLH are of orders ± 1. At least, the analytical prediction suggests that the first BPF tones are due to the main cyclic variations of angle of attack, whereas the higher harmonics are attributable to details ignored in the analytical model, such as tip vortices, influence of neighboring rotors, unsteady flow separations and so on.

2.4 Potential-Interaction Model

2.4.1 Blade-Loading Harmonics Induced by a Downstream Cylinder

This section is aimed at modeling the mean-flow distortion upstream of a strut or beam supporting a rotor, with a minimum mathematical effort, for estimating the induced blade-loading harmonics F_s. Closed-form expressions are searched in priority. The cylinder of circular cross-section is considered as generic geometry for beams, whereas arbitrary shapes are encountered in practice. It is argued that the upstream streamlines do not differ dramatically between true shapes and a cylinder, as long as the beam cross-section admits a unambiguous osculating circle. The analytical flow-distortion model is two-dimensional, based on the classical incompressible solution for the potential flow around a circle. The two-dimensional character can be an advantage if beams of non-constant cross-section are considered, and split into segments to comply with a strip-theory approach of rotor noise.

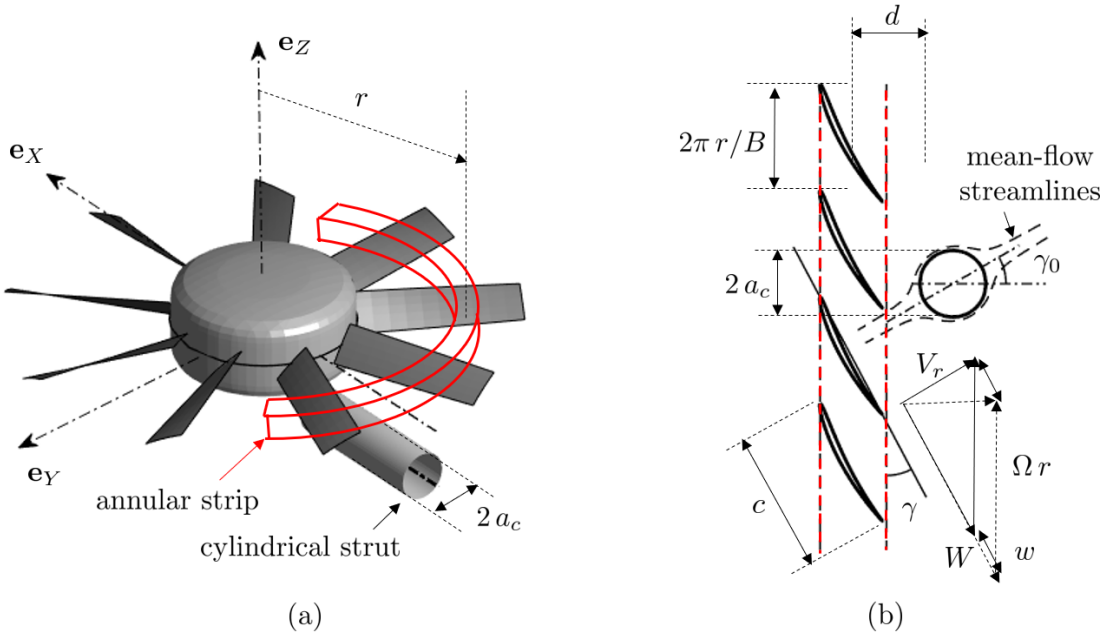


Figure 11: (a): Rotor-strut configuration, featuring in red the annular strip unwrapped in subplot (b), with notations in the Cartesian reference frame.

The expressions of the velocity components in the axial and tangential directions, in an unwrapped representation of a strip of arbitrary radius, as illustrated in Fig. 12, read (see Roger et al. (2006))

$$\frac{u(r,\phi)}{-V_r\,a_c^2} = \frac{d^2 - r^2\sin^2\phi}{[d^2 + r^2\sin^2\phi]^2}\,\cos\gamma_0 + 2d\frac{r\sin\phi}{[d^2 + r^2\sin^2\phi]^2}\,\sin\gamma_0\,,$$

$$\frac{v(r,\phi)}{-V_r\,a_c^2} = \frac{\cos\phi(d^2 - r^2\sin^2\phi)}{[d^2 + r^2\sin^2\phi]^2}\,\sin\gamma_0 - d\frac{r\sin 2\phi}{[d^2 + r^2\sin^2\phi]^2}\,\cos\gamma_0\,,$$

with γ_0 denoting the flow swirl angle with the rotor axis and γ being the blade pitch angle. (r, ϕ) are the polar coordinates along the mean circle of the considered strip (part of which is featured in red in Fig. 12-a). The vertical coordinate in Fig. 12-b is $r\phi$. In fact, the intersection of the strip with the cylinder is assimilated to a perpendicular cut of the cross-section of the cylinder. The approximation is valid as long as the diameter of the cylinder remains small compared to the blade-segment circular path.

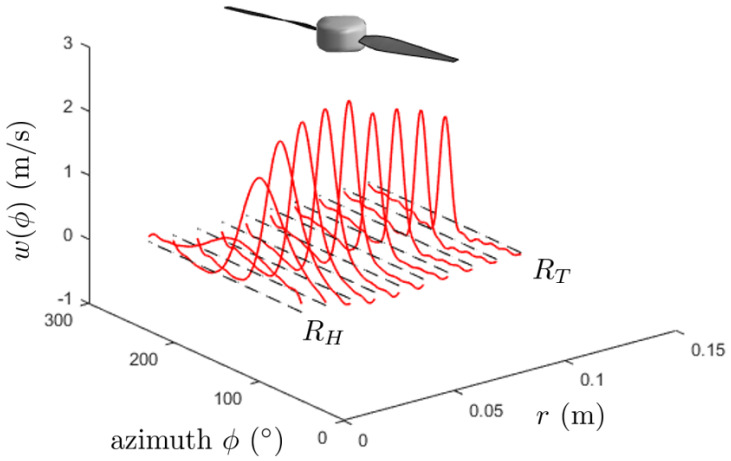


Figure 12: Upwash patterns on 9 strips for one blade of the 2-bladed rotor modeled by Roger and Moreau (2020).

The components $u(r, \phi)$ and $v(r, \phi)$ are experienced by the blade segment as an upwash, defined as the projection of the velocity disturbance normal to the chord. The distortion is stationary but the upwash is a relative time variation in the reference frame of the blade segment. Once this upwash is expressed for each strip, it is made periodic with an infinite sum in the unwrapped representation, in order to reproduce the angular periodicity. Its Fourier series provides distortion harmonics w_s. Each distortion harmonic triggers the blade-loading harmonic F_s of same order, via an unsteady aerodynamic transfer function. In view of its approximations, the model has a limited range of validity. As noted by Roger and Kucukcoskun (2019) in a typical shrouded tail-rotor architecture, the distortion harmonics produced by the Fourier series of upwash similar to the signals in Fig. 12 have the approximate form

$$w_s \;=\; (a_R - \mathrm{i}\, a_I)\, (-1)^s\, s\, \mathrm{e}^{-s/b}\,, \tag{18}$$

where b is increasing with the stagger angle γ at constant interaction distance, and a_R and a_I respectively decreasing and increasing, $(a_I^2 + a_R^2)^{1/2}$ being nearly constant. Though different trends could be observed for small-size drone rotor blades, the expression can be retained as a consistent general trend. The final intermediate step needed for tonal noise estimates is the derivation of the BLH from the coefficients w_s, for instance using Sears' theory.

It is worth noting that the rotor-strut interaction also includes sources of loading noise distributed on the cylinder surface and diffracted by the rotor blades, in other words the

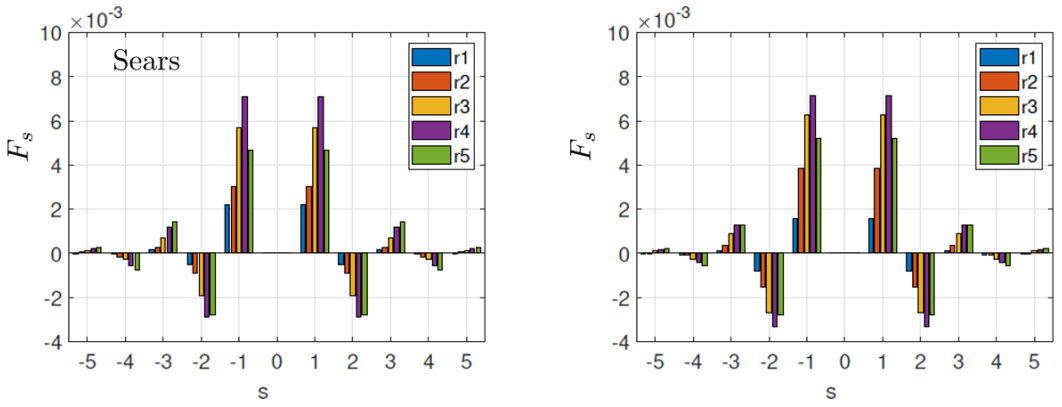
complementary aspects to those considered above. A dedicated two-dimensional quasi-steady analytical model was recently implemented by Vella et al. (2024), based on a potential approach. The principle is to assimilate the lifting cross-section of a blade to a point circulation, assumed successively at various positions with respect to the cross-section of the cylinder to simulate the blade passage, and to determine the flow by the complex-potential theory, as initially proposed by Wu et al. (2022). Other considerations on the rotor-cylinder arrangement will be given in section 3.3.3.

2.4.2 Propeller-Wing Interaction

As for other mechanisms, the specific interactions taking place as a puller propeller is installed in front of a wing deserve attention. Propeller noise caused by the potential flow distortion around the wing leading-edge appears as the dominant source of sound, but the localized impact of the propeller slipstream onto the wing surface must also be assessed. In particular, this contribution is modelled by acoustic dipoles normal to the wing surface. As such, they *a priori* radiate dominantly in vertical directions, which can complement flyover noise at relative extinction angles of propeller noise. A similar problem is the interaction of a propeller with a downstream pylon. A low-order prediction scheme coupling models for various identified contributions is described, for instance, by Akiwate et al. (2022). Many assumptions were made, to allow fast, repeated approximate calculations. The propeller blades and the wing were assumed unswept and made of thin plates. In fact, the arrangement was considered as a rotor-stator stage with two vanes on the stator, or equivalently as a contra-rotating system in which the rear-rotor was made of two blades and not rotating. This allowed the authors to simply adapt previous source models developed for Contra-Rotating Open Rotors (CROR), based on the same background as Amiet's response models and the potential-interaction model of section 2.4.1[3]. The propeller axis was assumed in the wing-chord plane, the surrounding medium was assumed at rest, and classical simplifications in linearized unsteady aerodynamic theories were accepted. The reference presents an example of aggregate models, each of which was previously developed for a dedicated mechanism, and combined with linear-superposition principles. It is typical of what the analytical approach is aimed at. A more elaborate panel method is also used by Mukherjee and Brentner (2020) to investigate the coupled aerodynamics of a flat-plate wing and ideal puller propeller.

These references are cited in the present section to give a flavor of the variety of modeling approaches, but they are not detailed. Again, the configuration B2 of ENODISE project is mentioned to illustrate only one aspect, namely the semi-analytical modeling of the BLH induced by the pylon of the single propeller-pylon unit already described in the lecture *Aeroacoustic Installation Effects in Propulsion Systems*. In Fig. 13 of this lecture, mean-velocity components are extracted from two planes located upstream and downstream of the propeller disc. The point in analytical modeling of BLH, typically using Sears' theory and available velocity disturbances, is to properly define the input of Sears' model. In the present case, quite logically, the computed velocity fields from

[3]For instance, without going into details, Amiet's approach based on Schwarzschild's technique is equivalent to the Wiener-Hopf technique, in the sense that the same mathematical statement is made, in terms of iterative solving of half-plane scattering problems. Furthermore, potential interactions are formulated on the common basis of the two-dimensional steady flow, around either a circle or an ellipse.



(a) from computed distortion (b) from computed blade forces

Figure 13: Blade-loading harmonics of an isolated propeller of EN-ODISE project, configuration B2, installed on its pylon. As deduced from computed distortion and Sears' theory (a), and as directly processed from computed blade forces (b). Five blade segments labeled by their increasing radii r_j, real part only.

the two extraction planes have been averaged, then distortion harmonics calculated by angular Fourier series, and finally BLH obtained in the same way as in the aforementioned tail-rotor case. The interest is that the BLH were also directly accessible from the CFD, by processing blade-surface pressure data, providing another, *a priori* much more accurate prediction. Both sets of results are shown in Fig. 13. Not only the overall agreement is very good, but the ranking of relative contributions of the five blade segments used to discretize a blade are reproduced by the semi-analytical approach. This proves that Sears' theory is reliable when only velocity distortions are available to characterize the interaction. Of course, this is only one part of the complete interaction problem, since the propeller slipstream also produces aerodynamic noise sources on the pylon.

It is worth noting that the results plotted in Fig. 13 are compatible with the general form given in Eq. (18), obtained from the two-dimensional model distortion around a cylinder. This suggests that the model can be transposed to a realistic configuration, for instance by defining an osculating circle for the leading-edge of the wing or pylon.

3 Acoustic Installation Effects

Analytical modeling of acoustic installation effects is the needed complement to that of the sound sources, or aerodynamic installation effects, in order to produce a complete prediction scheme, for early-design investigations. It is addressed in this section with the same background, namely the use of exact tailored Green's functions to generic geometries to formally solve the Helmholtz equation.

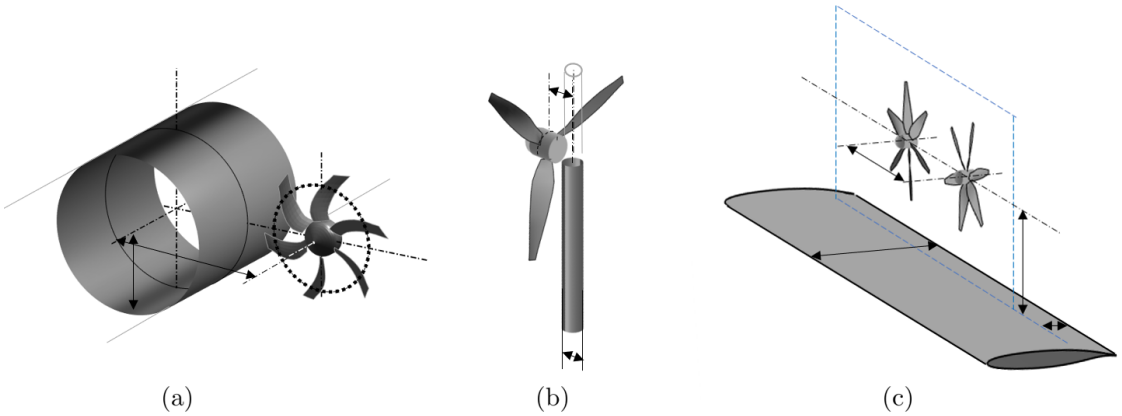


Figure 14: Generic configurations of propellers installed close to scattering surfaces. (a): propeller-fuselage, (b): rotor-beam, (c): wing-propeller (the rectangular wing can be replaced by a thin plate).

Basic generic configurations addressed in this section are sketched in Fig. 14, each mimicking a recognized installation effect.

3.1 Source-Mode Expansion

The analytical statement of diffraction problems is classically made in the frequency domain, based on Green's functions for the Helmholtz equation. The formalism is unable to account for source motion, the total acoustic field being derived for stationary sources characterized by their frequency content. This could appear as a stumbling block when addressing acoustic installation effects on rotating blades. Another aspect to consider is that scattering surfaces can be at arbitrary close distances from the sources in installed propeller/rotor architectures, making the far-field approximation insufficient. In this section, a mathematical identity is presented, by which the sound field of a single spinning radiation mode is equivalently reproduced by a continuous circular distribution of stationary phased dipoles. The equivalence is uniformly valid, for arbitrary source and observer positions, including near field. Green's formalism applied to each elementary source of this distribution will give access to the needed total field by linear superposition.

Consider a distribution of dipoles on a circle, such that the strength of the dipole at angle φ and at time t is $F(\varphi,t) = F(0, t-(mB-s)\varphi/(mB\,\Omega))$ with $F(0,t) = A\,\mathrm{e}^{-\mathrm{i}\,mB\,\Omega t}$. In the frequency domain at the angular frequency $mB\,\Omega$, the complex-valued dipole strength is $\tilde{F}(\varphi) = A_s\,\mathrm{e}^{\mathrm{i}\,(mB-s)\,\varphi}$. This obviously corresponds to the spinning mode of

order $(mB - s)$ and to the spinning phase speed $mB\,\Omega/(mB - s)$. The exact formula for a stationary point-dipole written in the spherical coordinate system, with origin at the centre of the source circle of radius r for the point dipole of arbitrary angle γ at angle φ, leads to the uniformly valid expression

$$p_s(\mathbf{x},\varphi) \;=\; A_s\,R\,\frac{(1-\mathrm{i}\,k_{mB}\,R(\varphi))}{4\,\pi\,R(\varphi)^3}\,\mathrm{e}^{\mathrm{i}\,[k_{mB}\,R(\varphi)+(mB-s)\,\varphi]}$$

$$\times\,\{\sin\gamma\sin\theta\,\sin(\phi-\varphi)-\cos\gamma\cos\theta\}$$

where $R(\varphi)$ stands for the exact distance from the source point to the observer. Then integrating over the circle, the complete sound pressure radiated anywhere including the near field is obtained. Equivalently it reads

$$p_s(\mathbf{x}) \;=\; A_s\int_0^{2\pi}\frac{(1-\mathrm{i}\,k_{mB}\,R(\varphi))}{4\,\pi\,R(\varphi)^3}\,\mathrm{e}^{\mathrm{i}\,[k_{mB}\,R(\varphi)+(mB-s)\,\varphi]} \tag{19}$$

$$\times\,\{\sin\gamma\,(Y\cos\varphi-X\sin\varphi)-Z\cos\gamma\}\;\mathrm{d}\varphi$$

once expressed in terms of the observer coordinates (X, Y, Z).

A far-field approximation can be derived after manipulations as

$$p_s(\mathbf{x}) \;=\; \frac{\mathrm{i}\,k_{mB}\,(2\,\pi)\,A_s}{4\,\pi\,R}\,\mathrm{e}^{\mathrm{i}\,k_{mB}\,R}\,(-\mathrm{i})^{(mB-s)}\,\mathrm{e}^{\mathrm{i}\,(mB-s)\,\phi} \tag{20}$$

$$\times\,\left[\cos\theta\cos\gamma-\frac{(mB-s)\,\sin\gamma}{k_{mB}\,r}\right]\,\mathrm{J}_{mB-s}\,(k_{mB}\,r\,\sin\theta)$$

Therefore comparing Eqs. (20) and the equations presented in the lecture *Review of aeroacoustic analogies and applications to UAM* shows that the former expresses the field of a single radiation mode from the infinite sum on the BLH, by identifying $A_s = BF_s/(2\pi)$. By virtue of its properties, the continuous array of phased dipoles can be called a source-mode. The source-modes can be used to synthesize the sound field of rotating blades. In practical implementations, each source-mode is discretized as a circular array of a sufficiently large number of point dipoles.

Examples of instantaneous sound-pressure maps for free-field source-modes in their plane are shown in Fig. 15, for the same arbitrary angular frequency ω. The number of angular periods, or lobes, n is indicated on the plots. The associated spinning phase speed is ω/n. Two regimes are recognized, one of efficient radiation with well structured spiral wavefronts and another one with evanescent character, the pressure amplitude decreasing very fast away from the source circle. In fact, evanescent and efficiently radiating modes correspond to vanishing and non-zero values of the Bessel functions involved in the far-field expression of the tonal noise. A key aspect of compact scattering, as illustrated in following sections, is that it dramatically enhances the radiation as a scattering surface enters the area of non-zero sound pressure of evanescent modes. This regime will be referred to as amplification, though it is more rigorously a mechanism of sound regeneration: the cancellation between spots of over-and under-pressures distributed along the source circle is de-activated because only some of the spots are modified by the scattering. In contrast, efficiently radiating modes will experience classical reflection/diffraction, with no strong increase of the total radiated power.

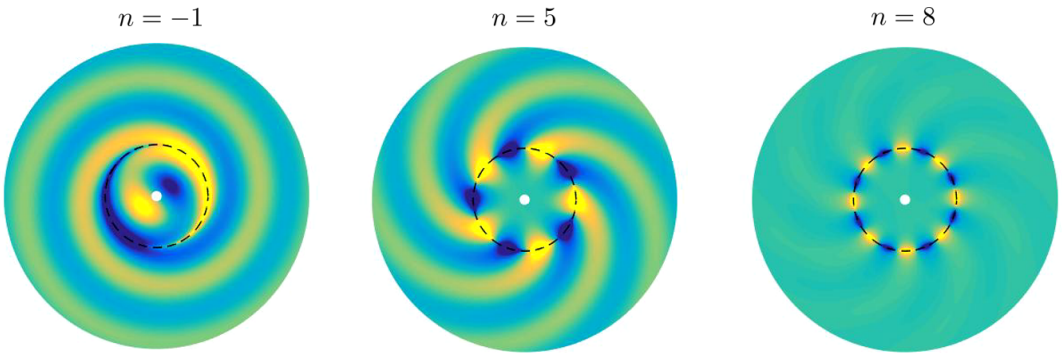


Figure 15: Typical sound-pressure wavefront patterns of source-modes in free field. Instantaneous maps in the plane of the source circle, featured as the dashed line. Over- and under-pressures as yellow and blue areas. All 3 modes at the same arbitrary frequency, same arbitrary color scale.

3.2 Edge Scattering and the Rigid Half-Plane Green's Function

3.2.1 Half-Plane Green's Function

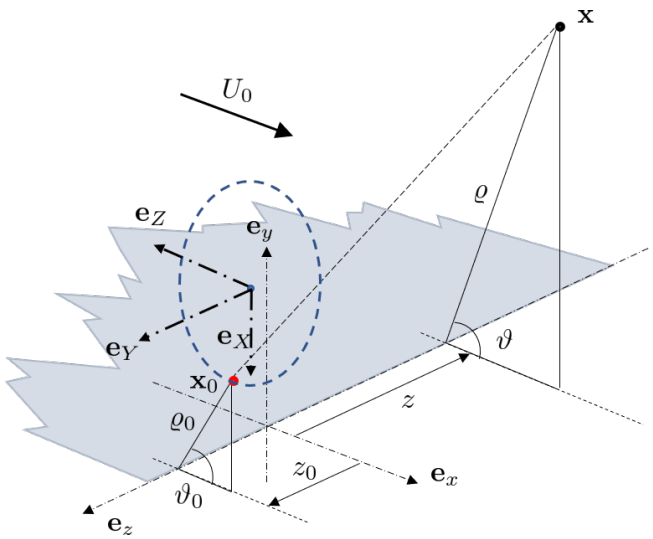


Figure 16: Reference frame and main notations for derivations based on the half-plane Green's function. Source-mode representative of a propeller added as dashed circle.

The exact expression of the rigid half-plane Green's function for the Helmholtz equation was first derived by Macdonald (1915) in a medium at rest. If expressed in cylindrical coordinates for a source point $\mathbf{x}_0 = (\varrho_0, \vartheta_0, z_0)$ and an observer at point $\mathbf{x} = (\varrho, \vartheta, z)$, with the z axis along the edge and ϑ being π along the half-plane and zero in its contin-

uation (Fig. 16), it reads

$$\mathrm{G}_{1/2}^{(0)}(\mathbf{x},\mathbf{x}_0) \;=\; \frac{-\mathrm{i}k}{4\,\pi^2}\left\{\int_{-\infty}^{u_0}\frac{\mathrm{K}_1^*(ik\,R_1\sqrt{1+u^2})}{\sqrt{1+u^2}}\,du \;+\; \int_{-\infty}^{u_1}\frac{\mathrm{K}_1^*(ik\,R_2\sqrt{1+u^2})}{\sqrt{1+u^2}}\,du\right\} \quad (21)$$

where $k=\omega/c_0$ is the acoustic wave number and the upper bounds are given by

$$u_{0,1} \;=\; \pm\frac{2}{R_{0,1}}\,(\varrho\,\varrho_0)^{1/2}\,\cos\frac{\vartheta\mp\vartheta_0}{2}$$

with

$$R_{0,1} \;=\; \left[\varrho^2+\varrho_0^2+(z-z_0)^2-2\,\varrho\varrho_0\cos(\vartheta\mp\vartheta_0)\right]^{1/2}\;.$$

K_1 is the modified Bessel function of order 1, equivalently written in terms of the Hankel function as $\mathrm{K}_1^*(\mathrm{i}\xi)=-(\pi/2)\mathrm{H}_1^{(1)}(-\xi)$.

The extension to the presence of a uniform mean flow along the half-plane and perpendicular to the edge, needed to consider forward flight if the half-plane is mimicking the trailing-edge of a wing, is obtained by simply applying Lorenz's transform. Introducing the mean-flow Mach number M_a, and keeping the reference frame attached to the half-plane, the so-called convected Green's function is obtained as

$$\mathrm{G}_{1/2}^{(M_a)}(\mathbf{x},\mathbf{x}_0) \;=\; \frac{1}{\beta_a}\,\mathrm{e}^{-\mathrm{i}kM_a\,(x-x_0)/\beta_a^2}\,\mathrm{G}_{1/2}^{(0)}(\mathbf{X},\mathbf{X}_0) \quad (22)$$

in which $\mathbf{X}$ and $\mathbf{X}_0$ are coordinate vectors, the streamwise coordinate of which x has been replaced by $X=x/\beta_a$, the wavenumber being rescaled as $K=k/\beta_a$ with $\beta_a=\sqrt{1-M_a^2}$. No Kutta condition is imposed in this framework, but the question was treated in two dimensions by Jones (1972) and Rienstra (1981). Other aspects are discussed by Roger et al. (2016).

The exact acoustic field of a point dipole of strength $\mathbf{F}$ is given by the scalar product $\mathbf{F}\cdot\nabla\mathrm{G}_{1/2}^{(0)}$. Therefore Eq. (21) and its extention are the basis for deriving the uniformly-valid radiated field of source-modes, accounting for the diffraction by the edge, at the price of a numerical treatment of the integrals and derivatives with respect to the source coordinates.

The behavior associated with compact scattering is often analyzed from the asymptotic form of the Green's function for a far-field observer and a source point in the very near field of the edge, which reads

$$\mathrm{G}_{1/2}^{(0)}(\mathbf{x},\mathbf{x}_0) \;\simeq\; \frac{\mathrm{e}^{\mathrm{i}\,kR}}{R}\left\{1+2\frac{\mathrm{e}^{\mathrm{i}\pi/4}}{\sqrt{\pi}}\,(2\,k\varrho_0\sin\phi)^{1/2}\,\sin\frac{\vartheta_0}{2}\,\sin\frac{\vartheta}{2}\right\}\;. \quad (23)$$

The space derivatives needed to calculate the far-field sound from dipoles have the effect of discarding the factor 1 inside the curly brackets and of generating factors $(k\varrho_0)^{-1/2}$. This causes the characteristic amplification of compact scattering.

3.2.2 Edge Scattering of Propeller Noise: Sample Results

Sample results are illustrated in Fig. 17-a, for the elementary source-mode of order $n=2$, frequency 1 kHz and radius $R_s=0.2$ m, at horizontal and vertical distances to the

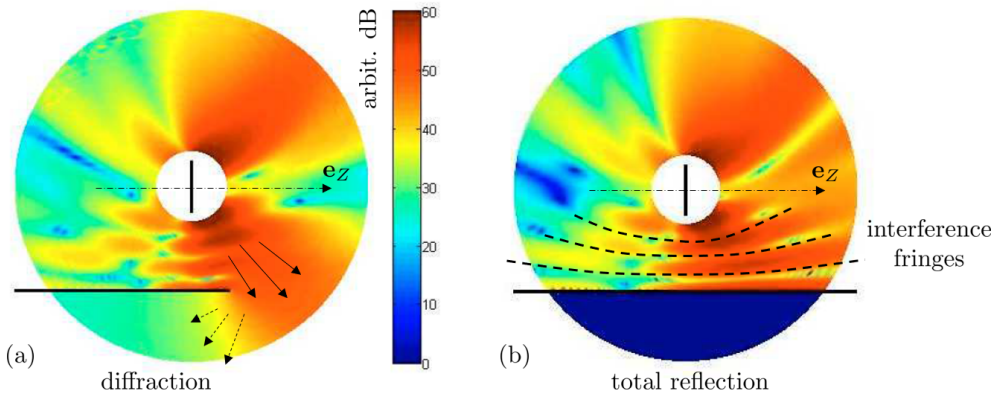


Figure 17: Typical SPL maps of a single radiation mode; uniformly valid Green's function implementation, from Roger (2007). Side view, source-mode circle seen as the vertical segment. Spinning mode $n = 2$, frequency 1 kHz. (a): horizontal and vertical distances to the edge $1.5\,R_s$ and $3\,R_s$ (R_s circle radius: 0.2 m). (b): same mode, reflection by an infinite rigid ground. Propagation medium at rest.

edge $1.5\,R_s$ and $3\,R_s$, respectively. The plotted quantity is the sound pressure level, in arbitrary decibel scale. The natural oblique lobes characteristic of the free-field signature of the mode, as well as the extinction along the axis, are clearly recognizable. The most striking feature is that the downward main lobe impinges almost directly on the edge, which gives rise to significant sound regeneration in the shadow region (left bottom quadrant of the figure). This condition must be avoided as far as possible to get benefit of the masking expected from simple geometric considerations. The radiation pattern is compared to what the same mode would produce at the distance $3\,R_s$ from an infinite rigid ground (Fig. 17-b). The solution is simply provided by the image principle in this case. A significant regeneration of sound is seen around the positive Z axis, because of the reflection. Furthermore, interference fringes are clearly identified, marked by the dashed curved lines. It is worth noting that the upper left part in Fig. 17-a is close to that in Fig. 17-b, because the reflection is the dominant mechanism in this area.

3.2.3 Green's Function Approximation by Truncation

When the diffraction of sources by the edge(s) of a strip of finite chord must be addressed, considering an infinite span in a first step, the half-plane Green's function is questionable. Indeed, it ignores the diffraction by the other edge of the strip. For sources located closer to a trailing edge in practice, this second contribution is coming from the leading edge and is qualified, quite arbitrarily, as back-scattering. We keep this definition, addressing architectures in which a propeller is installed closer to the trailing edge of a wing. Facing the lack of exact Green's function for the infinite strip, an intuitive

truncation procedure is proposed here for simplicity[4]. The justification is found in general Green's integral formulations of a radiation problem in the presence of rigid surfaces, noted $\mathcal{S}$, for which a tailored Green's function is known. The general expression of the total sound field reads

$$p(\mathbf{x}) = \int_{\mathcal{V}} S(\mathbf{y})\, \mathrm{G}_k(\mathbf{x},\mathbf{y})\, \mathrm{d}\mathbf{y} - \int_{\mathcal{S}} p(\mathbf{y})\, \frac{\partial \mathrm{G}_k}{\partial n}\, \mathrm{d}\mathbf{y}\,, \tag{24}$$

for any Green's function G_k and a known source term $S(\mathbf{y})$. If the free-space Green's function G_0 is used, the volume integral term denotes the direct field (free-field) from the sources, and the surface integral is the scattered field, seen as the direct field of secondary dipole sources. A second expression is obtained by choosing the tailored Green's function G for G_k, the surface integral vanishing by definition, because G satisfies the rigid-wall boundary condition. This provides an explicit value of $p(\mathbf{y})$ by making $\mathbf{x}$ go onto the surface in this second expression. Once used as input in the first expression, with G_0, this value allows to calculate the scattered field from the surface integral. Of course, both obtained derivations of the pressure field are equivalent. But a different result is obtained if the surface integral is only considered on a part of the surface instead of the total surface. If the major scattering effect is attributable to the secondary dipoles distributed within the area preserved by the truncation, the result is expected close to what the exact scattering by the truncated surface would be.

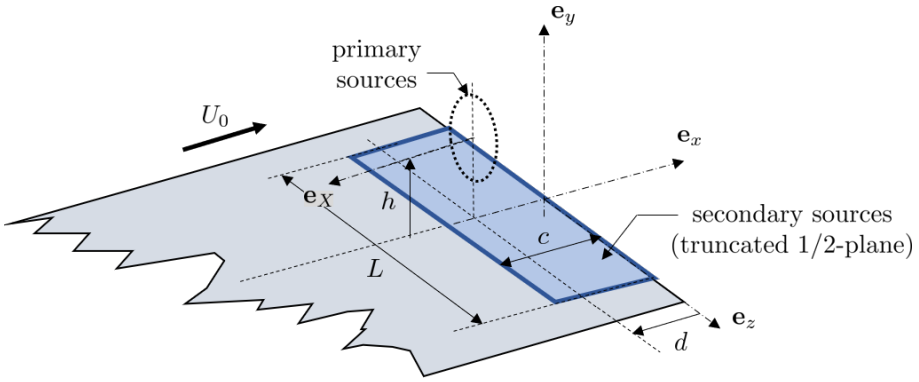


Figure 18: Reference frame and main notations for edge-scattering formulations. Truncation of the rigid half-plane featured in blue.

This idea was applied to the configuration of a rectangle by Acevedo-Giraldo et al. (2022). It is illustrated in Fig. 18. Once secondary sources are known over the entire half-plane, their radiation calculated using the free-space Green's function equivalently reproduces the scattered field. Truncating the half-plane to only consider the rectangle of finite span L and chord c in the procedure provides an approximation of the scattering by the mimicked wing. The approximation is believed acceptable for primary sources located in the vicinity of the trailing edge, and for non-compact chord lengths. Two-dimensional tests made with point dipoles and a thin rigid segment confirmed the validity of the approximation, by successfully comparing with a FEM (Finite Element Method)

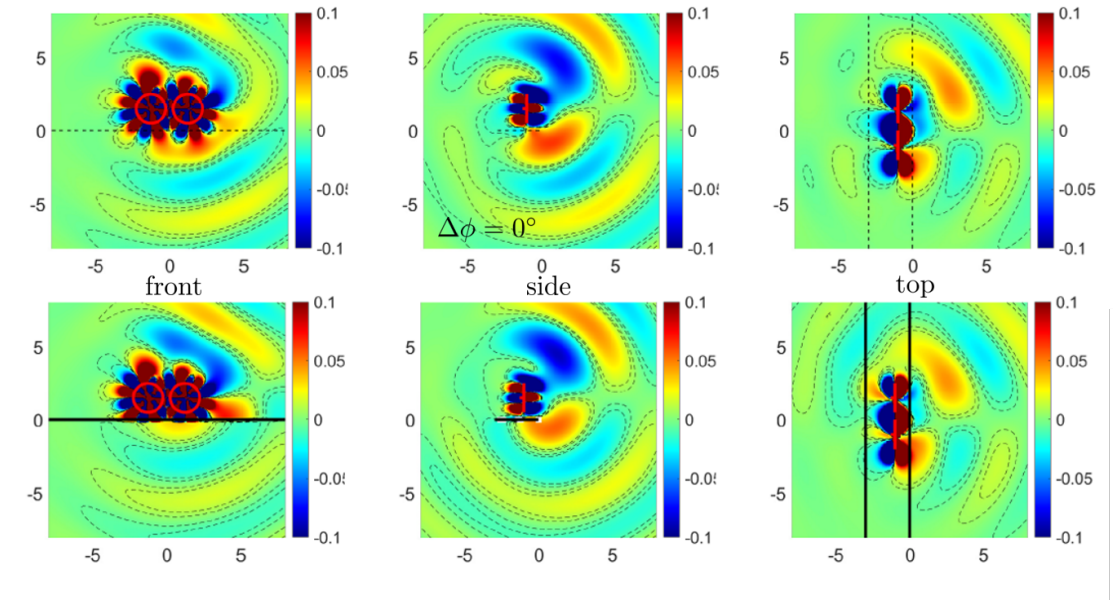
[4]Note that a high-frequency solution exists for the diffraction of a plane wave, based on the Wiener-Hopf technique. Yet it is also approximate, and only meaningful for sources at arbitrary large distances.

solver (see Acevedo-Giraldo et al. (2022)). This was used in the ENODISE project to investigate the scattering of the tonal noise from a pair of side-by-side propellers installed close to the trailing-edge of a wing (configuration B2). The axis-to-axis distance between the propellers, their either co- or contra-rotating arrangement, as well as the normal and streamwise distances to the edge, h and d respectively, have been changed, looking for the best theoretical configuration for sound masking. But the model was also used to determine the range of parameters, for which amplification of the direct sound field is produced, because of the compact-Green's function behavior.

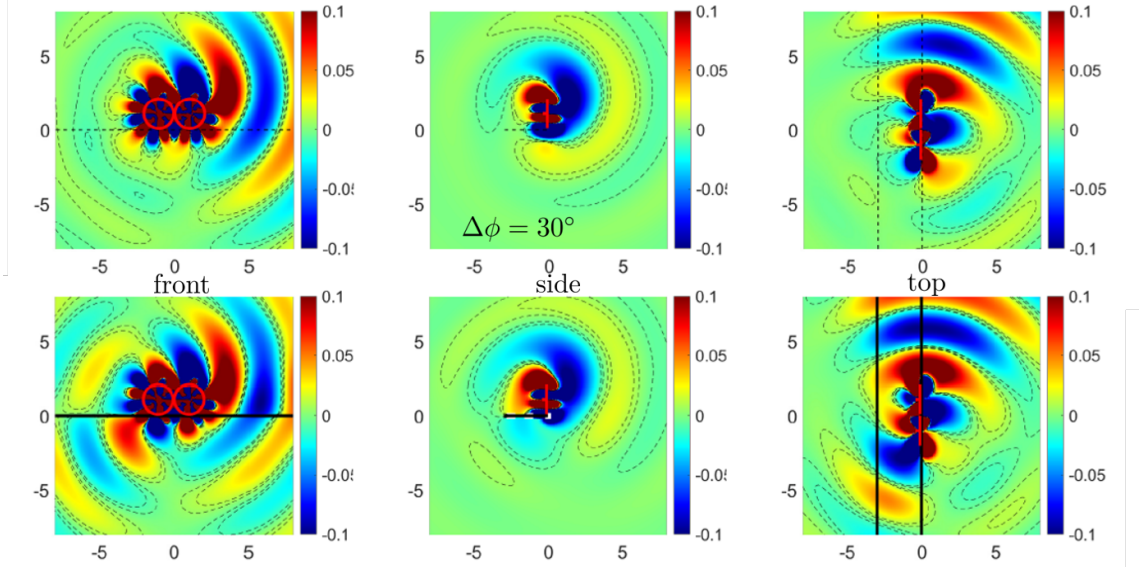
As illustration, instantaneous acoustic pressure wavefronts, predicted using the approximate Green's function of the wing and the BLH deduced from the computed velocity distortion shown in the lecture *Aeroacoustic installation effects in propulsion systems* are presented in Fig. 19, for two configurations of the pair of co-rotating propellers. Figure 19-a reports on a configuration of efficient sound masking, the propellers being removed from the vicinity of the trailing edge, and Fig. 19-b on the configuration of sound amplification by compact edge scattering, obtained with minimum distance to the edge. Upper plots display the free-field sound pressures, and lower plots the total fields in the presence of the rectangular strip mimicking the wing. The wing position is indicated by the dotted and plain lines, respectively. The three projections, namely a front view in the propeller plane, a side view and a top view in the plane of the wing, are needed to appreciate the scattering effect. Indeed, the sources of the scattered field are dipoles normal to the wing surface, thus not contributing in its plane. The propellers are clockwise-rotating in the front view, and different synchrophasing $\Delta\phi$ is imposed in both cases, indicated in the figure.

It is worth noting that the amplification evidenced as part of a source-mode circle approaches the edge to compact distances does not operate on broadband noise. Indeed, tonal-noise source-modes are circular distributions of dipoles of zero instantaneous balance. In that sense, they tend to be equivalent to sources of higher polar orders (quadrupoles and higher) if their radius is also close to compactness. Edge scattering introduces imbalance, thus regenerates sound that should be partly suppressed by cancellation between elementary dipoles. The complete coherence of the circular distribution of sources is a necessary condition for amplification. Uncorrelated distributions of dipoles radiate without disturbed imbalance.

Finally, an example of complete analytical prediction, chaining a source model and a sound-scattering model, is compared to the experiment in Fig. 20, again in some cases of the ENODISE configuration B2. The case is that of two synchrophased propellers, with the same positioning parameters of efficient masking as in Fig. 19-a (see Fig. 19 of lecture *Aeroacoustic installation effects in propulsion systems*). Both contra-rotating (CTR) and co-rotating (COR) propeller pairs are considered. The BLH are assumed the same as in Fig. 13. Therefore, additional lift fluctuations on the blades due to the mean-flow downwash by the wing is ignored, as well as the effect of propeller-propeller interaction. But these effects are believed minimized in this selected case (sufficient distance to the wing edge and separation between propellers), so that the potential interaction with the pylon is the dominant mechanism. Thus the same sources are simply duplicated on both propellers. In Fig. 20, the sound level at the BPF is plotted as two complementary directivity diagrams, in the mid-span (horizontal) plane and in a plane close to that of the propeller discs (vertical). The symbols stand for the measured values, and the plain



(a)



(b)

Figure 19: Predicted instantaneous sound-pressure patterns for the pair of co-rotating propellers tested in ENODISE configuration 2. Selected extreme cases of efficient masking (a) and of amplification by edge scattering (b). Free field on top rows and total fields on bottom rows. Wing position indicated by solid-line segments. Propeller blade-tip circles in red..

lines for the predictions. The contra-rotating arrangement is obviously found the noisiest. The overall agreement of predictions with measurements is very satisfactory, despite some local discrepancies. The most striking fact is that the model is able to predict the relative

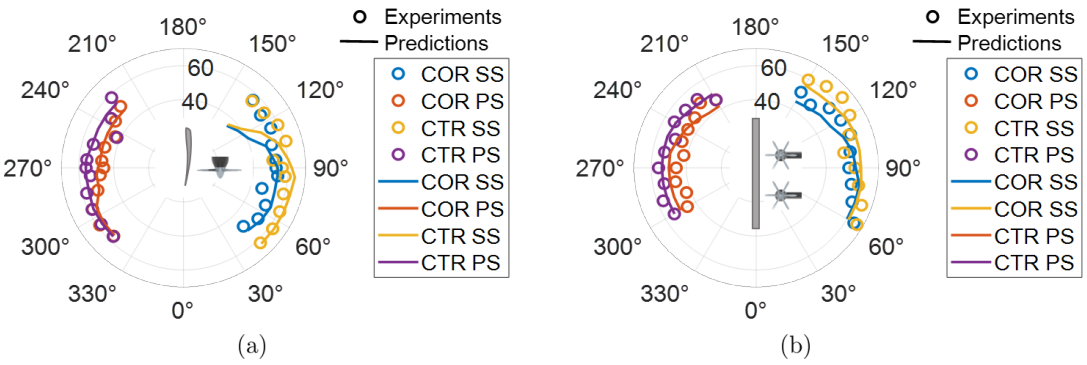


Figure 20: Comparison of measured (symbols) and analytically predicted tone levels at the BPF (lines), in the ENODISE configuration B2. Case of efficient masking. (a): mid-span plane; (b): plane perpendicular to wing chord.

variations, which is the most important required quality when searching for optimum configurations. Causes for the discrepancies could be the neglected additional distortions, and maybe spurious scattering effect on the nozzle, at some observation angles.

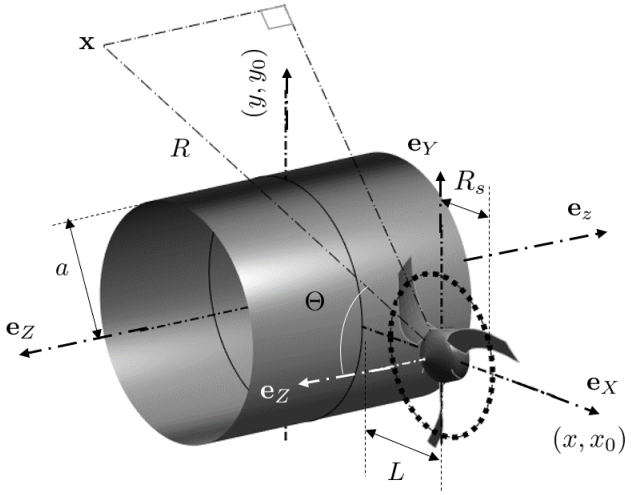


Figure 21: Notations and reference frames used for derivations based on the cylinder Green's function. Case of propeller noise scattering by the fuselage of an aircraft.

3.3 The Green's Function of the Rigid Cylinder

3.3.1 General Expression

Two generic configurations can be built, based on the Green's function of the rigid cylinder. The first one is that of a propeller installed beside the fuselage of an aircraft,

in which case the cylinder and propeller axes are parallel. The second one is that of a rotor supported by a radial beam or strut, and in this case the two axes are perpendicular to each other. The common background is the expression of the Green's function given by Morse and Feshbach (1953), generalized to the presence of a uniform flow parallel to the axis by Kingan and Self (2012) (see also Kingan (2014)). With the notations in Fig. 21, it can be written as

$$\mathrm{G}(\mathbf{x},\mathbf{x}_0) \;=\; \frac{\mathrm{i}}{4\pi}\int_0^\infty \sum_{m=0}^{\infty} a_m \,\cos[m(\theta-\theta_0)]\,\cos[k_z(z-z_0)] \qquad (25)$$

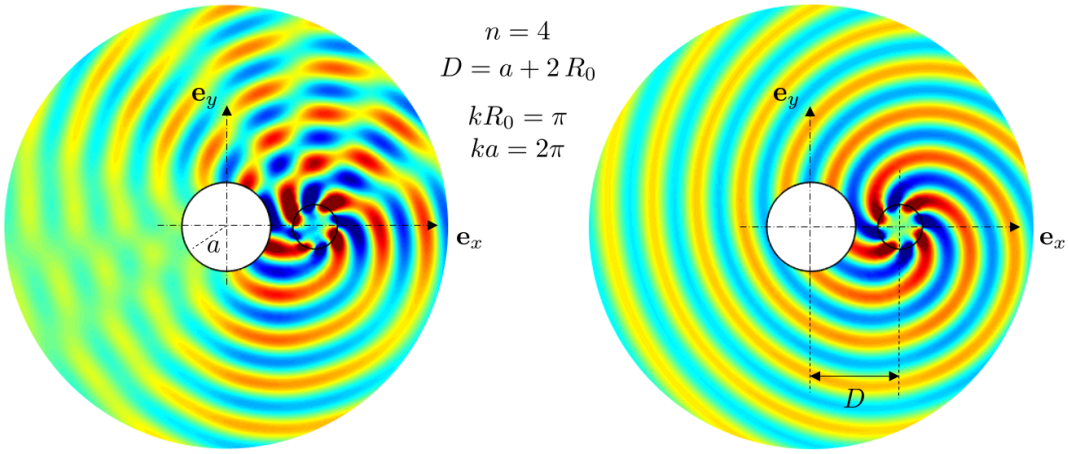
$$\times\,\Big[\mathrm{H}_m^{(1)}(\gamma\, r)\;\big(\mathrm{J}_m(\gamma\, r_0)-\beta_m(\gamma\, a)\,\mathrm{H}_m^{(1)}(\gamma\, r_0)\,\big)\Big]\;\mathrm{d}k_z\,,$$

with

$$\gamma \;=\; \sqrt{k^2-k_z^2}\,, \qquad \beta_m(\gamma\, a) \;=\; \frac{\mathrm{J}_{m-1}(\gamma\, a)-\mathrm{J}_{m+1}(\gamma\, a)}{\mathrm{H}_{m-1}^{(1)}(\gamma\, a)-\mathrm{H}_{m+1}^{(1)}(\gamma\, a)}\,.$$

a_m is 1 for $m=0$ and 2 otherwise. $\mathbf{x}=(r,\theta,z)$ denotes the observer and $\mathbf{x}_0=(r_0,\theta_0,z_0)$ a source point on the circle, expressed in cylindrical coordinates with reference at the center of the cylinder cross-section. It must be noted that the propeller reference frame $(\mathbf{e}_X,\mathbf{e}_Y,\mathbf{e}_Y)$ and the cylinder reference frame $(\mathbf{e}_x,\mathbf{e}_y,\mathbf{e}_z)$ have different orientations.

The Green's function of the rigid cylinder is written here for the Helmholtz equation in a medium at rest. The extension to the presence of uniform flow along the axis is straightforward; it keeps the basic physics unchanged, at the price of a slight shift of frequency, not addressed here for conciseness.



(a) total field (b) direct field

Figure 22: Scattering of an elementary source-mode of propeller noise by a fuselage. (a): instantaneous sound-pressure pattern in the plane of the mode, in a non-compact configuration. Parameters indicated on the plots. (b): direct field only.

3.3.2 Non-Compact Case of a Fuselage

A test-case of implementation is shown in Fig. 22. The instantaneous sound pressure of the mode $n = 4$ is calculated in the plane of the mode, including a cross-section of the fuselage. The values of Helmholtz numbers indicated on the plots correspond to a non-compact case. The free-field (Fig. 22-b) features the spiral wavefronts characteristic of an efficiently radiating mode. In the presence of the cylinder, a significant masking is predicted. Furthermore, the scattered and direct fields interfere in a complex way. This results in the formation of multiple directivity lobes separated by extinction angles, but only in the upper part of the map. This top/bottom imbalance is due to the counterclockwise-rotating character of the mode. The extinctions and lobes would be formed in the lower half-space for a clockwise-rotating mode. Would the mode be evanescent in free field, with concentrated spots of over- and under-pressures distributed along the source circle and remaining far enough from the cylinder surface, nothing significant would be generated in terms of scattering.

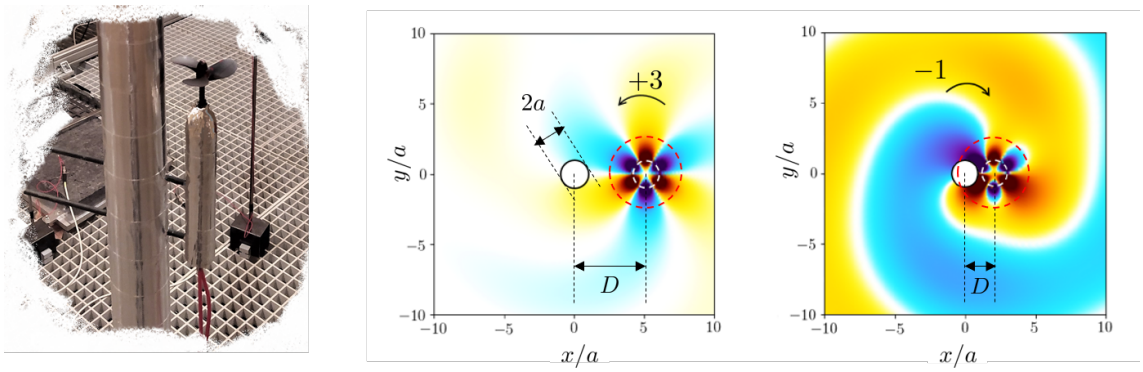
These features are typical of large passenger aircraft, but different behavior is expected from architectures of smaller dimensions.

3.3.3 Cases of Compact Scattering

A totally opposite situation to the previous one is faced if now the cross-section of the cylinder and the circle of the source-mode are together embedded in a compact area, smaller than the acoustic wavelength (also if the source-mode radius significantly exceeds the radius of the beam cross-section). The regime of compact scattering is entered. It is the usual framework of the low-frequency tonal noise emitted by marine propellers, addressed in particular by Cros et al. (2023). A key result from the reference is reproduced in Fig. 23. The spinning mode $n = 3$ is selected, as representative of the free-field of the steady-loading noise of the propeller, said rotor-locked mode. This mode is not efficient, because of the low tangential Mach number. Indeed, the over- and under-pressure spots decrease rapidly away from the source-mode circle, in Fig. 23-b. In this subplot, the cylinder is not entering the area of large amplitude of the spots, therefore the scattered field is of negligible amplitude. In contrast, as the interaction distance is reduced, so that the cylinder enters this area, as pictured in Fig. 23-c, a strong increase of sound is observed, with the formation of the contra-rotating mode $n = -1$. This is exactly what was found in the experiment, as discussed in section 3.2.1 of the lecture *Aeroacoustic installation effects in propulsion systems*. Asymptotic derivations in the reference were shown to explain the strong amplification observed experimentally, with the following outcomes:

- the source-modes of orders 0 and ± 1 are not amplified by compact scattering;
- higher-order modes are increasingly amplified as their order is increased, but of course their intrinsic efficiency in free field is decreasing;
- the scattered field of amplified higher-order modes is strongly dominated by the contra-rotating mode of order 1, for any incident mode order.

It is clear that these findings lead to reconsider the noise from marine propellers, irrespective of any other aspect, such as structural vibrations, that are not negligible in water. But the experiment was performed in air, with a very small propeller of 6 cm diameter, and dimensional considerations make the amplification effect also expected in other con-



(a) (b) (c)

Figure 23: Two-dimensional implementation of the cylinder Green's function in the compact propeller-cylinder configuration reported by Cros et al. (2023). (a): picture of the experiment. (b-c): simulated instantaneous sound-pressure patterns, for the direct propeller mode $n = 3$ at relatively large (b) and short (c) distances of the cylinder.

figurations of low characteristic Helmholtz numbers. In particular, small-size drones, with two-bladed rotors of diameters of the order of 10-to-20 cm have typical blade-passing frequencies around 150-200 Hz, thus diameter-based Helmholtz numbers below 1. Moreover, the rotor-beam distances of interaction are much smaller, of a couple of centimeters. This suggests that the compact regime of sound scattering is reached, motivating dedicated investigations. But the generic configuration mimicking a propulsive unit of drone or eV-TOL aircraft is rather made of a radial beam, thus only extending over half the diameter. Therefore, the diffraction does not operate on diametrically opposed parts of the source-mode circles of the tonal noise. Again, the truncation procedure based on Eq. (24) and introduced in section 3.2.2 can be repeated to account for this. The Green's function of the infinite cylinder is used to determine the secondary dipoles of the scattered field, only half of which are retained to synthesize the total field.

Model analytical predictions are reported in Fig. 24, for the first four modes $n = 0$ to 3, assumed representative of the tonal noise of a drone rotor, all of same radius and at the same distance from a cylindrical strut. Two options are compared, namely a diametrical cylinder and a radial cylinder extending only over half the diameter. Only the second one is representative of real rotor-beam arrangements. Both are mimicked by infinite and semi-infinite cylinders, respectively. Three meshed surfaces are superimposed, for the direct field (black), and for the total fields with the infinite cylinder (purple) and with the semi-infinite one (red). All diagrams are plotted with the same arbitrary decibel scale. The mode $n = 0$ is almost unaffected by the scattering, and the effect on the mode $n = 1$ is very weak. As compact circular sources, both can be considered as dipoles, respectively vertical and stationary for the mode $n = 0$ and horizontal and spinning for the mode $n = 1$. But higher-order modes have the character of sources of higher polar order. The radiation from the mode $n = 2$ is strongly increased, with a very significant level around the $\mathbf{e}_Z$ axis. Indeed, the over/under-pressures of this mode are diametrically symmetrical. They induce secondary sources on the diametrical cylinder, of equal phase on each side

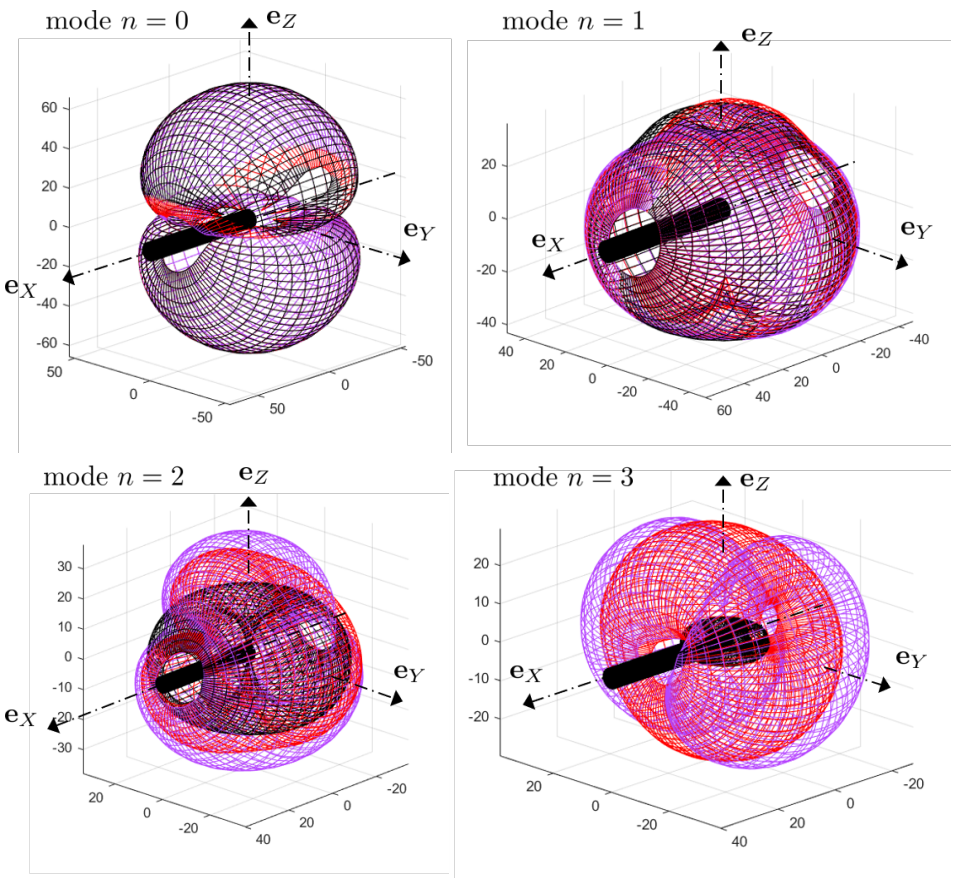


Figure 24: 3D-directivity patterns of single rotor source-modes emitting above a radial or diametrical cylindrical strut. Parameters representative of small-size drones. Direct field (black), total field with diametrical (purple) and radial (red) cylinders.

of the axis. More sound is radiated with the diametrical cylinder than with the radial one. The behavior of the mode $n = 3$ is totally different, because it is characterized by diametrical over/under-pressures of opposite phases. Therefore, they induce secondary sources of opposite phases on each side of the axis on the infinite cylinder, which produces an extinction around the source-mode axis. The resulting purple pattern of the mode $n = 3$ features an equivalent dipole of axis $\mathbf{e}_Y$. No such extinction can be produced with the semi-infinite cylinder. Anyway, with the parameters of the test, representative of a small-size drone, the direct field of the mode $n = 3$ is dramatically small compared to its total field. The sound essentially emanates from the cylinder, no longer from the source-mode.

Recent numerical simulations of a generic rotor-cylinder configuration of low Helmholtz number, performed with an incompressible LES solver and reported by Gojon et al. (2023) and Vella et al. (2024), confirm the surface of the cylinder as the dominant source of dipole sound radiation. Furthermore, the predicted sound, using the CFD as input to Ffowcs Williams & Hawkings equation, compared very well with the experiment. Because by definition, such simulations are unable to reproduce acoustic mechanisms, this suggests that the much higher sound heard as the rotor-beam distance is reduced is rather an aero-

dynamic installation effect. Now the amplification of source-modes by compact scattering is mathematically proved in the present section, as an acoustic installation effect. This apparent paradox is presently under investigation. It could be explained by the fact that, within a compact domain, the Helmholtz equation tends to be equivalent to the Laplace equation, which can be verified if coordinates are made dimensionless by the extent of the domain.

References

Acevedo-Giraldo, D., Roger, M., Jacob, M., and Bériot, H. (2022). Analytical study of the aerodynamic noise emitted by distributed electric propulsion systems. In *28th AIAA/CEAS Aeroacoustics Conference*, paper 2022-2830, Southampton.

Akiwate, D., Parry, A., Joseph, P., and Paruchuri, C. (2022). Analytical investigation of propeller-wing interaction noise. In *28th AIAA/CEAS Aeroacoustics Conf., Aviation 2022*, paper 2022-2877, Southampton.

Amiet, R. (1975). Acoustic radiation from an airfoil in a turbulent stream. *J. Sound & Vib.*, 41:407–420.

Amiet, R. K. (1976). Noise due to turbulent flow past a trailing edge. *J. Sound & Vib.*, 4(3):387–393.

Arroyo Ramo, A., Alguacil, A., Moreau, S., Bauerheim, M., and Jacob, M. (2024). Artificial neural networks prediction of wall-pressure spectrum. In *30th AIAA/CEAS Aeroacoustics Conf.*, paper 2024-3140, Rome.

Bertagnolio, F., Madsen, H. A., Fischer, A., and Bak, C. (2017). A semi-empirical airfoil stall noise model based on surface pressure measurements. *J. Sound & Vib.*, 387:127–162.

Carazo, A., Roger, M., and Omais, M. (2011). Analytical prediction of wake–interaction noise in counter-rotating open rotors. In *17th AIAA/CEAS Aeroacoustics Conference*, Paper 2011–2758, Portland OR.

Cerny, M. and Breitsamter, C. (2020). A comparison of isolated and ducted fixed-pitch propellers under non-axial inflow conditions. *Aerospace*, 7(8):112.

Christophe, J., Anthoine, J., Rambaud, P., and Moreau, S. (2008). Numerical issues in the application of an amiet model for spanwise-varying incoming turbulence. In *14th AIAA/CEAS Aeroacoustics Conference*, paper 2008-2865, Vancouver.

Cros, E., Roger, M., and Serre, G. (2023). Low-frequency amplification of propeller tonal noise due to the scattering by a compact rigid cylinder. *J. Sound & Vib.*, 546:17450.

Gojon, R., Parisot-Dupuis, H., Mellot, B., and Jardin, T. (2023). Aeroacoustic radiation of low reynolds number rotors in interaction with beams. *JASA*, 154:1248–1260.

Goldstein, M. (1976). *Aeroacoustics*. McGraw-Hill NY.

Graham, J. (1970). Similarity rules for thin airfoil in non-stationary subsonic flow. *J. Fluid Mech.*, 43(4).

Grasso, G., Jaiswal, P., Wu, H., Moreau, S., and Roger, M. (2019). Analytical models of the wall-pressure spectrum under a turbulent boundary layer with adverse pressure gradient. *J. Fluid Mech.*, 877:1007–1062.

Hunsaker, D. and Snyder, D. (2006). A lifting-line approach to estimating propeller/wing interactions. In *24th AIAA Applied Aerodynamics Conference*, page 3466.

Jones, D. (1972). Aerodynamic sound due to a source near a half-plane. *IMA J. of Appl. Math.*, 9(1):114–122.

Kingan, M. (2014). Open rotor centrebody scattering. *J. Sound & Vib.*, 333:418–433.

Kingan, M. and Self, R. (2012). Open rotor tone scattering. *J. Sound & Vib.*, 331:1806–1828.

Lee, S. (2018). Empirical wall-pressure spectral modeling for zero and adverse pressure gradient flows. *AIAA J.*, 56(5):1818–1829.

Macdonald, H. (1915). A class of diffraction problems. *Proc. Lond. Math. Soc.*, 2(1):410–427.

Mish, P. and Devenport, W. (2006). An experimental investigation of unsteady surface pressure on an airfoil in turbulence, part 1: effects of mean loading. *J. Sound & Vib.*, 296(3):417–446.

Misiorowski, M., Gandhi, F., and Oberai, A. (2019). A computational study on rotor interactional effects for a quadcopter in edgewise flight. *AIAA J.*, 57:5309–5319.

Moreau, S. and Roger, M. (2009). Back-scattering correction and further extensions of Amiet's trailing-edge noise model. part ii: Application. *J. Sound & Vib.*, 323(1-2):397–425.

Morse, P. and Feshbach, H. (1953). *Methods of Theoretical Physics, part I.* McGraw-Hill.

Mukherjee, B. and Brentner, K. (2020). Investigation of propeller-wing interaction noise and the potential contribution to evtol noise. In *VFS Tech. Conf. Aeromech. Design for Transformative Vertical Flight*, San Jose, CA.

Paterson, R. and Amiet, R. (1976). Acoustic radiation and surface pressure characteristiccs of an airfoil due to incident turbulence. Technical report, NASA CR 2733.

Phillips, W. F. and Snyder, D. O. (2000). Modern adaptation of prandtl's classic lifting-line theory. *Journal of Aircraft*, 37(4):662–670.

Rienstra, S. (1981). Sound diffraction at a trailing edge. *J. Fluid Mech.*, 108:443–460.

Roger, M. (2007). Near-field fan noise modeling and installation effects due to scattering surfaces. In *Fan Noise 2007*, paper 57.

Roger, M. (2010). On broadband jet-ring interaction noise and aerofoil turbulence-interaction noise predictions. *J. Fluid Mech.*, 653:337–364.

Roger, M. (2013). Broadband noise from lifting surfaces, analytical modeling and experimental validation. In *Noise sources in turbulent shear flows, fundamentals and applications, CISM series 545*, pages 0000–xxxx. R. Camussi, Springer.

Roger, M. and Kucukcoskun, K. (2019). Near-and-far field modeling of advanced tail-rotor noise using source-mode expansions. *J. Sound & Vib.*, 453:328–354.

Roger, M. and Moreau, S. (2005). Back-scattering correction and further extensions of Amiet's trailing-edge noise model. Part 1: Theory. *J. Sound & Vib.*, 286(3):477–506.

Roger, M. and Moreau, S. (2010). Extensions and limitations of analytical airfoil broadband noise models. *Int. J. of Aeroacoustics*, 9(3):273–305.

Roger, M. and Moreau, S. (2020). Tonal-noise assessment of quadrotor-type uav using source-mode expansions. *MDPI Acoustics*, 2(3):674–690.

Roger, M., Moreau, S., and Guédel, A. (2006). Vortex-shedding noise and potential-interaction noise modeling by a reversed Sears' problem. In *12th AIAA/CEAS Aeroacoustics Conference*, paper 2006-2607, Cambridge MA.

Roger, M., Moreau, S., and Kucukcoskun, K. (2016). On sound scattering by rigid edges and wedges in a flow, with application to high-lift device aeroacoustics. *J. Sound & Vib.*, 362:252–275.

Rozenberg, Y., Robert, G., and Moreau, S. (2012). Wall-pressure spectral model including the adverse pressure gradient effects. *AIAA J.*, 50(10):2168–2179.

Schulten, J. B. (1996). Advanced propeller performance calculation by a lifting surface method. *Journal of propulsion and power*, 12(3):477–485.

Sears, W. (1941). Some aspects of non-stationary airfoil theory and its practical application. *J. Aeronaut. Sciences*, 8(3).

Sinayoko, S., Kingan, M., and Agarwal, A. (2013). Trailing edge noise theory for rotating blades in uniform flow. *Proc. Roy. Soc.*, A:1–28.

Vella, E., Gojon, R., Parisot-Dupuis, H., Doué, N., Jardin, N., and Roger, M. (2024). Mutual interaction noise in rotor-beam configuration. In *30th AIAA/CEAS Aeroacoustics Conf.*, paper 2024-3318, Rome.

von Kármán, T. and Sears, W. (1938). Airfoil theory for non-uniform motion. *Journal of the Aeronautical Sciences*, 10(5):379–390.

Wu, Y., Kingan, M., and Go, S. (2022). Propeller-strut interaction tone noise. *Phys. of Fluids*, 34:055116.